Journal of the Iranian Chemical Society
https://doi.org/10.1007/s13738-023-02781-2

ORIGINAL PAPER

Amino acid-capped transition metal ion-doped iron oxide nanoparticles: evaluating drug delivery carrier efficiency and in vitro magnetic resonance image contrasting ability

Bindi Sanghavi[1] · Sucheta De Mondal[1] · Urja Verma[2] · Suresh Balakrishnan[2] · Sk Riyajuddin[3] · Kaushik Ghosh[3] · Mitesh Sarkar[4] · Hemant P. Soni[1]

Received: 25 August 2022 / Accepted: 26 February 2023

Abstract

L-arginine capped and transition metal-doped Ultra-Small Iron Oxide Nanoparticles (USIONs) were synthesized by a wet chemical method. The nanoparticles (NPs) were encapsulated with Pluronic F127® and used as a vehicle (M^{2+}/Fe_3O_4@L-Arg/P) to load anti-cancer drug. The interaction of ligand molecules with NPs surface was studied by FTIR spectroscopy, while the Vibrating Sample Magnetometry and Mössbauer spectroscopy were used for magnetic properties. In vitro, drug release kinetics showed that Mn^{2+}/Fe_3O_4@L-Arg/P/bg release 30% drug initially within 5 h and the next 20% in 72 h with an overall 50% release in three days. Approximately, 70% drug was released from Ni^{2+}/Fe_3O_4@L-Arg/P/bg. The Mn^{2+}/Fe_3O_4@L-Arg/P/bg took a long time to 70% release rate than Zn^{2+} and Ni^{2+}-doped vehicles. M^{2+}/Fe_3O_4@L-Arg/P/bg with 10 µg/mL dosage can reduce the cell viability to 53, 31, and 94 for Zn^{2+}, Mn^{2+}, and Ni^{2+}, respectively. Contrasting ability of the material was evaluated for Magnetic Resonance Imaging (MRI). The results indicate a shift from inherent T_2 to T_1 contrasting with a lower concentration. The parameters (like $\tau_{M,}$ $\tau_{R,}$ q, etc.) used in Solomon–Bloembergen–Morgan (SBM) theory for paramagnetic relaxation also be applicable to Fe_3O_4-based NPs system in terms of H-bonding to modulate the T_1 contrasting in MRI.

Graphical Abstract

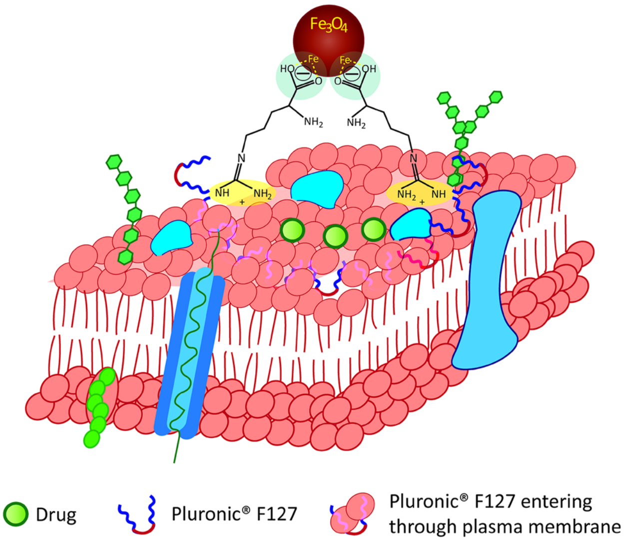

Ultra-Small Iron Oxide Nanoparticles are designed for theranostic applications. Both the core and the shell environment of the nanoparticle assembly can be modulated to achieve optimum performance in terms of drug delivery and contrasting effect under magnetic field.

Extended author information available on the last page of the article

Keywords MRI contrast agent · Drug delivery vehicle · Ultra-Small Iron Oxide Nanoparticles · Magnetic theranostic agents · Relaxation time

Abbreviations

USIONs	Ultra-Small Iron Oxide Nanoparticles
Fe_3O_4@L-arg	NPs-L-arginine-capped Fe_3O_4 nanoparticles
Fe_3O_4@L-arg/P	NPs-L-arginine-capped and Pluronic F-127-enveloped Fe_3O_4 nanoparticles
M^{2+}/Fe_3O_4@L-arg/P	NPs-transition metal-doped L-arginine-capped and Pluronic F-127-enveloped Fe_3O_4 nanoparticles
NPM	Nuclear phosphoprotein B23, numatrin
EML4	Echinoderm microtubule-associated protein-like 4

Introduction

Iron oxide-based materials find unique applications in modern science, particularly in the areas like drug delivery, cellular imaging, development of MRI contrast agents (CAs), hyperthermia induction, biosensing, and protein separation [1–3]. The advantages of using magnetite for these applications are that it is non-toxic and decomposes into iron acting as an iron pool required for the synthesis of hemoglobin during erythropoiesis [4]. In bulk form, magnetite is paramagnetic having a large number of magnetic domains oriented randomly in absence of an applied magnetic field. On application of a magnetic field, they orient themselves in a single direction and revert to the random state on the removal of the field. However, it leaves some residual magnetization (ferrimagnetic behavior) which is not desirable for applications like MRI contrast agents (CAs) or drug delivery platforms [5, 6]. It was observed that by decreasing the particle size to about 20 nm, these domains merged into a single domain having one collective magnetization direction on applying the field and, further, immediately got demagnetized on the removal of the field (superparamagnetic behavior) [7, 8]. Any material having this property is perfect to serve as a drug delivery vehicle. However, by decreasing the particle size, magnetic material has a natural tendency to agglomerate [9, 10]. The ferro-fluid having a very less particle size in a given solvent system is unstable. To make a stable suspension and prevent agglomeration, the surface of the particle is coated with molecules of surface active agents like CTAB, SDS, etc. However, such suspension shows toxicity at physiological pH. Hence, the surfactant-free synthesis of Fe_3O_4 nanoparticles (NPs) is desired [11, 12].

Very few iron oxide-based MRI CAs are available in the market globally (e.g., Ferridex®, Endorem®, and Resovist®) as compared to Gd-based CAs, even though there is an abundance of research reported in this area [13, 14]. The main reasons are (i) magnetite NPs commonly act as T_2 CAs (darkening the lesions) by interrupting the signals coming from the lesions, and this requires more processing time compared to Gd-based T_1 CAs (brightening the lesions), (ii) the dark lesions very often confused with other pathogenic situations like hemorrhages, fat deposits or calcification which necessitate supplementary pathological data to conclude the disease [15–17], (iii) their prolonged half-life in the body requires weeks to a month time to get cleared from the blood utilizing phagocytosis through macrophages (e.g., Kupffer cells) followed by uptake by the liver, spleen, and lymph nodes. In contrast, Gd complexes get cleared from the body within minutes creating the contrast effect immediately post the entry into the target [18–20], (iv) their physical properties vary with particle size, and (v) the uniform particle size (monodispersity) of the suspension is crucial. It is achieved by adopting the synthesis route involving non-aqueous coordinating solvents (dodecane, oleylamine, etc.) at high temperature compels stringent experiment control [21], resulting in water-insoluble ferrofluid. A tedious procedure like ligand exchange through dialysis for more than 24 h is required to make the material hydrophilic and water soluble [22]. However, incomplete ligand exchange hampers the stability in aqueous media. Despite all these drawbacks, the attraction for the development of iron oxide-based theranostic agents remains intact. Affordable, non-toxic, and water-soluble magnetic theranostic agents can be developed by amending these process parameters [23].

The research in this area gets momentum when it was observed that iron oxide NPs having less than 5 nm particle size show T_1 contrasting ability (ES-MIONs) [24, 25]. This is due to suppressed magnetization along a longitudinal axis which decreases r_2 relaxivity and enhances r_1 by diminishing the spin canting effect at a very small particle size. It is clear from this discussion that image contrasting ability can be adjusted by tuning the particle size of the Fe_3O_4 NPs. These can be achieved, in the case of Fe_3O_4, by fine-tuning the magnetic interactions among Fe^{2+}/Fe^{3+} ions at crystal lattice sites. Bulk Fe_3O_4 NPs (80–100 nm) possess a high magnetic moment (80–120 emu/g) which distorts the background noise resulting in confused image contrasting [26]. Due to this, a very small cancerous lesion cannot be detected (e.g., early stage of cancer) or over-sighted [27]. These difficulties can be solved by modulating the magnetic moment of the NPs by doping with suitable ions.

Brigatinib is a second-generation anaplastic lymphoma kinase (ALK) inhibitor known to be an effective pharmacological agent against numerous types of cancer. It is approved by the U.S. Food and Drug Administration for the treatment of non-small cell lung cancer (NSCLC) since April 2017 [28]. It acts to inhibit anaplastic lymphoma kinase (ALK), epidermal growth factor receptor (EGFR), and reactive oxygen species (ROS)—all of which are known drivers of NSCLCs [29]. It has been documented that ALK, ROS, and EGFR can induce a series of phosphorylation reactions responsible for the up-regulation of the oncogenes like NPM and EML4 [30]. Brigatinib is reported to block phosphorylation and prevents the progression of the cell cycle in cancerous cells [31]. The side-effects like diarrhea, nausea, abdominal pain, constipation, dizziness, fever, headache, trouble sleeping, joint pain, lowering of blood pressure, etc., due to high (or initial) dosage of brigatinib can be overcome when targeted delivery to the cancerous lesion carried out. In light of these, the anti-cancer activity of brigatinib was evaluated in vitro on a representative model of NSCLC epidermoid carcinoma cell line A431 on loading with various as-synthesized magnetite-based drug delivery vehicles.

In previous studies, we demonstrated that Fe_3O_4 NPs having the surface modified by suitable small amino acid molecule (L-proline) and enveloped by amphiphilic block copolymers such as Pluronic F-127 can be used as a vehicle to conjugate drug/gene [32, 33]. It is well established that such kind of platforms can effectively load and deliver the cargo to the target and also function as MRI CAs. Moreover, most of the syntheses reported to date are carried out in constrained conditions to stringently control the particle size and phase purity of the magnetite. However, during large-scale production, such conditions may not be strictly followed as some minute errors during unit operations could result in wastage of the total batch and make it economically unviable. In this study, we have synthesized Ultra-Small Iron Oxide NPs (Fe_3O_4-USIONs) and ferrites (MFe_2O_4) by a simple co-precipitation method and these L-arginine-modified and Pluronic F127®-coated Fe_3O_4 NPs (Fe_3O_4@L-Arg/P) evaluated as drug delivery platform and MRI CAs. We focused on tuning the intrinsic magnetic property of USIONs by varying the transition metal dopant ions under the same reaction conditions rather than adopting the solvothermal or any other tedious synthesis methods. We report, here, the tuning of magnetism and improvement as well as the reversal of contrasting ability by doping Fe_3O_4 with suitable transition metal ions (Zn^{2+}, Mn^{2+}, and Ni^{2+}). We have demonstrated by in vitro studies that doped magnetite shows higher drug delivery efficiency with improved performance as MRI CAs. It has been demonstrated that the parameters (like $\tau_{M,}$ $\tau_{R,}$ q, etc.) proposed in Solomon-Bloembergen-Morgan (SBM) theory for paramagnetic relaxation can also be applicable in the case of Fe_3O_4-based NPs system in terms of hydrogen bonding to modulate the T_1 contrasting in MRI.

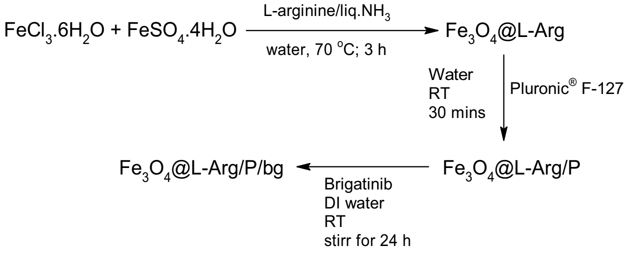

Scheme 1 An overall synthesis scheme of developed drug delivery vehicle and MRI contrast agents

Experimental

Materials

Ferric chloride $FeCl_3.6H_2O$, $ZnCl_2$, and $MnSO_4$ were obtained from Loba Chemicals, India. Ferrous chloride $FeCl_2.2H_2O$ and an aqueous solution of ammonia were purchased from S.D Fine Chemicals, India. Pluronic® F-127 and L-arginine were purchased from Sigma-Aldrich. All chemicals were of AR grade and used without further purification.

Synthesis of L-arginine coated magnetic nanoparticles (Fe_3O_4@L-Arg NPs)

Ferric chloride hexahydrate (5.0 g, 18.5 mmol) and ferrous sulfate tetrahydrate (2.4 g, 10.7 mmol), in a molar ratio of 1:0.58, were added to 250 mL deionized water under an inert atmosphere. The mixture was heated to 70 °C to a clear solution. The mixture was stirred vigorously with a mechanical stirrer to avoid interparticle magnetic interaction. After 30 min, L-arginine (8.01 g, 46.0 mmol), dissolved in 50 mL deionized water, was rapidly added. The reaction mixture was further stirred for 30 min. Then 27 mL ammonia (25%) was rapidly added which, in turn, changed the reaction color to black. The stirring was continued for 1.5 h. Finally, the black nanoparticles were separated magnetically, washed with distilled water thrice, and dried at 100 °C overnight (Scheme 1).

A dry weight of nanoparticles: 2.54 g.

Similarly, $Zn_xFe_{3-x}O_4$ ($x=0.2$)@L-arginine, $Mn_xFe_{3-x}O_4$ ($x=0.2$)@L-arg, and $Ni_xFe_{3-x}O_4$ ($x=0.2$)@L-arg were synthesized by adding a solution of $ZnCl_2$ (0.001 mol, 0.2689 g), $MnSO_4$ (0.001 mol, 0.151 g), and $NiCl_2$ (0.001 mol, 0.13 g) prepared in 30 mL DI water. (Yields range from 90 to 95%.)

Synthesis of brigatinib-loaded Fe_3O_4@L-Arg/P magnetic micelles (Fe_3O_4@L-Arg/P/bg)

In total, 300 mg of Fe_3O_4 NPs was dispersed in 30 mL of DI water and then 100 mg of Pluronic® F-127 was added. The mixture was then stirred overnight on a magnetic stirrer at RT and then centrifuged at 6000 rpm for 5 min to form Fe_3O_4@L-Arg/P NPs. In total, 30 mg of these NPs was dispersed in 10 mL of DI water. To it, 2 mL of the drug solution (4.5 mg mL^{-1}) was added and the mixture was stirred vigorously at RT for 24 h. The drug-loaded Fe_3O_4 NPs were allowed to settle down by a magnet. The drug-loaded NPs were suspended in DI water and washed twice (Scheme 1).

The same procedure was adopted for Zn^{2+}, Mn^{2+}, and Ni^{2+}-doped Fe_3O_4 NPs.

Characterization

X-ray powder diffraction (XRD) pattern of the Fe_3O_4@L-Arg NPs was obtained using an X-ray powder diffractometer (BrukerD8 Advance) with Cu Ka radiation, $\lambda=0.15418$ nm. The mode of interaction of L-arginine with the surface Fe ions of Fe_3O_4 NPs was studied by using Fourier Transform Infrared Spectroscopy (RX-FTIR, Perkin-Elmer, USA). The morphology of the samples was examined by Transmission Electron Microscopy (TEM, Philips Tecnai 20) at 200 kV. All measurements were taken at 25 °C in deionized water. Differential Scanning Calorimetry (DSC) analysis and Thermogravimetric Analysis (TGA) of Fe_3O_4@L-Arg and Fe_3O_4@L-Arg/P were carried out using a Mettler-Toledo DSC822. For this purpose, the material was heated inside a DSC setup at 10 °C min^{-1} from RT to 500 °C under an N_2 atmosphere. The Mössbauer spectra were recorded in the transmission geometry with a constant acceleration transducer and a 512-channel multichannel analyzer. A ^{57}Co (Rh) source of activity (10 mCi) was used. The line width of the spectrometer was 0.27 mm/s. The magnetic properties were studied by VSM (Lakeshore 7410) at 298 K under an applied magnetic field of $15.000\times10^{+3}$ G.

The amount of drug-loaded nanoparticles was calculated by using UV–visible spectroscopy. A drug solution in the concentration range from 0.5 to 9.0 mg mL^{-1} was prepared to construct a calibration curve. It was found that for every 1 mg of NPs, 0.096 mg of the drug was loaded out of 0.150 mg of the bare drug.

$$\text{Loading efficiency (\%)} = (\text{Weight of drugloaded}/\text{weight of total drug added}) \times 100 \tag{1}$$

$$\text{Drug loading \%} = \text{the mass of loaded drug} /\text{the mass of initial drug and carrier} \times 100 \tag{2}$$

The drug loading efficiency and drug loading percentages were 64.0 and 8.35%, respectively.

A phantom study was carried out to determine the relationship between T_1 and T_2 relaxation times with various concentrations of Fe_3O_4@L-Arg/P NPs. For the phantom preparation, aqueous solutions of NPs (0.5, 0.25, 0.1, 0.05, 0.01, and 0.001 mg mL^{-1}) were prepared and transferred into microcentrifuge tubes (2 mL). Pure water and L-arginine solution (1 mg/mL) were taken as references. An array of microcentrifuge tubes was placed in a plastic container with water for magnetic field homogeneity. The phantom was carefully placed in the center of the head coil, and MR imaging was performed at RT using a clinical 1.5 T GE Medical Systems scanner in combination with a 16-channel wrist joint coil. To determine the T_1 relaxation time of each concentration, spin-echo (SE) sequences with different repetition times (TR; 100, 200, 400, 600, 800, 1000, 2000, 3000 ms) and an echo time (TE; 15 ms) were performed. The other imaging parameters were as follows: slice thickness = 7 mm, the field of view (FOV) = 5 × 5 cm, matrix = 320 × 192, flip angle = 90°, and imaging time = 1.0 min.

For T_2 relaxation time, an SE protocol with the following parameters was used: TR = 3000 ms with TE = 9, 27, 36, 99 ms, and other parameters were the same as above. The signal intensity in arbitrary units (a.u.) for each of the imaging sequences was obtained using Dicom (digital imaging and communication in medicine) Works software v 1.3.5 (Dicom Works, Lyon, France) via locating a circular region of interest (ROI) in the center of each tube (maximum region of interest was considered). Recorded signal intensities were fitted in Excel (Windows 10) using exponential Eq. (3), and (4) to evaluate R_1 ($1/T_1$) and R_2 ($1/T_2$) relaxation rates, respectively.

$$\text{Signal}_{\text{SE}} = S_0\left(1 - e^{-\text{TR}/T_1}\right) \tag{3}$$

$$\text{Signal}_{\text{SE}} = S_0\left(e^{-\text{TE}/T_2}\right) \tag{4}$$

The slopes of R_1 and R_2 relaxations versus the concentration of the samples were calculated as relaxivity values r_1 and r_2 in Microsoft office 2007.

In vitro study design

The cell lines used in the experiment (A431 human epidermoid carcinoma cell line) were purchased from the National Center for Cell Science (Pune, India). Dulbecco's Modified Eagle's Medium (DMEM) with low glucose supplemented with 10% fetal bovine serum (FBS) with 1% antibiotic solution (penicillin and streptomycin) was used for the maintenance and healthy growth of the cells. The cells were cultured in a constant environment at 37 °C with 5% CO_2 in a humidified CO_2 incubator. A wide range of concentrations starting from 1 μg mL^{-1} to 1000 μg mL^{-1} was selected for the in vitro study as in the initial screening; the formulations were found to cause almost complete mortality at higher doses. The range selected was 1, 2, 3, 4, 5, 6, 7, 8, 9, 10, 100, 200, 500, 750, and 1000 μg mL^{-1}. The details of the experiment are described as follows.

In vitro drug release kinetics

To study the drug release kinetics, three different experiments were performed. This study was carried out at 37 °C and pH 7.4. In each experiment, 3.0 mg of brigatinib-loaded magnetic NPs was added to a flask having 30 mL of Na_2HPO_4–NaH_2PO_4 buffer solution. The flask was then kept in a shaker at 37 °C. The release medium was withdrawn at predetermined time intervals (1, 2, 3, 4, 5, 6, 7, 8, 9, 12, 24, 36, 48, 60, 80, 100, 124, 148, 172, and 196 h). The collected samples were analyzed using a UV–Vis spectrophotometer (Perkin-Elmer Lambda 35) to determine the amount of brigatinib released (λ_{max} 284 nm).

In vitro cytotoxicity test

The cytotoxicity of all the samples was tested on an A431 epidermoid carcinoma cell line by a 3-(4, 5-dimethylthiazol-2-yl)-2,5-diphenyltetrazolium bromide (MTT) assay (Sigma-Aldrich, USA). In complete full-growth media, A431 cells were seeded in a 96-well plate (5×10^3 cells per well). Then, cells were treated with Fe_3O_4@L-arg NPs, brigatinib-loaded NPs, and pristine brigatinib of the same amount as loaded on NPs for 48 h at 37 °C. After 48 h, the MTT was added to each well and the cells were incubated at 37 °C for 4 h. The medium was removed and dimethyl sulfoxide (DMSO) was added to dissolve the formazan crystals. The absorbance was measured at 570 nm with a Microplate Reader (iMark, BioRad, USA). The experiments were performed in triplicate. The relative cell viability (RCV) w.r.t. the control wells were calculated by the following equation: $RCV = (OD_{test}/OD_{control}) \times 100\%$, where OD_{test} and $OD_{control}$ were obtained in the presence and absence of the NPs, respectively.

Clonogenic assay

We used a clonogenic assay to determine the colony-forming ability of cells under the effect of different treatments. For this assay cells were seeded in 6-well plates at their log phase. A thousand cells per well were plated and incubated in the total media (DMEM low glucose, 10% FBS, 1% antibiotic solution). These were treated with the M^{2+}/Fe_3O_4@L-Arg/P/bg and bared brigatinib drugs for 48 h. The medium was then replaced with new media without any added drugs or formulations. Colonies were stained with crystal violet after 5 days of treatment. The number of colonies containing at least 50 cells was counted using the ImageJ software (NIH, USA). The percentage of colonies formed was calculated by dividing the number of colonies by a product of the number of cells plated and the plating efficiency. Data were obtained in triplicates and graphs were prepared in GraphPad PRISM software (San Diego, CA, USA).

Results and discussion

Structure and morphology elucidation

We have strategically selected L-arginine a small molecular capping ligand to arrest particle growth due to its zwitterionic property. Out of its different resonance structures, the one having a positive charge distributed over the guanidinium nitrogen and a negative charge over the carboxylate group predominated under synthesis conditions. The negatively charged carboxylate ion can easily coordinate with the surface Fe^{2+}/Fe^{3+} ions of Fe_3O_4 NPs rendering the overall surface hydrophilic. Now, the positively charged guanidinium group remains projected outside the surface which, in turn, orients the drug molecules around it by H-bonding. The hydrophobic part of the drug molecules forces the next Pluronic® F127 layer to assemble in such a way that its hydrophobic PPO blocks remain tucked inward, while the hydrophilic PEO blocks on the outside form a normal hydrophilic micellar surface (Fig. 1A) [34]. It is very well recognized from previous studies that a Pluronic shell can provide a stealth outer layer to the delivery vehicle, enabling it to sustain itself while encountering all the physiological barriers through its journey into the target cells [35]. L-arginine is a non-toxic amino acid and immediate precursor of NO, an important signaling molecule having a crucial function during the immune response to the infection [36]. Once inside the cell, lysosomal degradation of the assembly releases L-arginine with iron compounds. These released residues aid the function of brigatinib by inducing an immune response and thereby hastening cell apoptosis. Since L-arginine binds with brigatinib through H-bonding only during the drug loading stage, the release of the drug

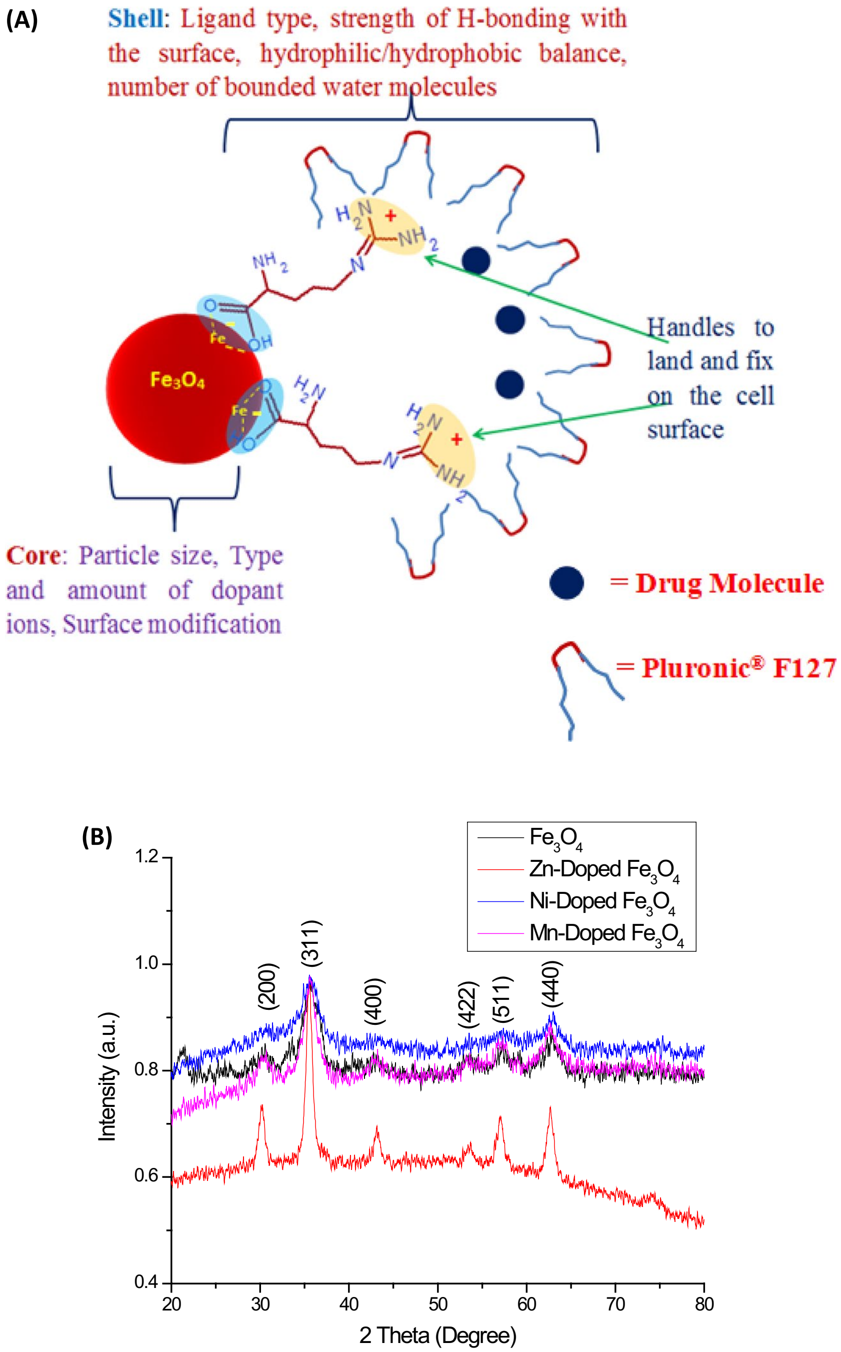

Fig. 1 **A** Cartoon showing Fe_3O_4@L-Arg/P/bg NPs magnetic micelle as a drug delivery vehicle. The parameters to tune the magnetic relaxation for MRI, enhance the drug loading and cell transfection. **B** XRD pattern of the as-synthesized M^{2+}/Fe_3O_4@L-Arg nanoparticles

occurs smoothly at the target without any change in its molecular structure.

It can be seen from Fig. 1A that the relaxation rate for T_1 imaging can be tuned in two ways: Firstly, the particle size of the Fe_3O_4 NPs can be adjusted up to 10 nm with the magnetism tuned by doping with the suitable dopant ions. This, in turn, can influence the dipole–dipole interactions with the inner sphere water protons relaxing faster in the presence of an applied field. Secondly, the selection of ligands for surface coordination of NPs is very important as it creates a hydrophilic shell environment by forming an inner sphere of H-bonded water molecules. The strength of H-bonding with water molecules depends on the hetero atoms present in the molecular structure of the ligand (discussed further in the Phantom study). Finally, this core@shell structure is encapsulated in a polymeric micelle formed by PEO-PPO block copolymeric surfactant, Pluronic®F127 (during the synthesis, the amount of pluronic adjusted was above CMC, i.e., 20 mg/mL to ensure the formation of a polymeric micelle) [37]. Now, when this nanoassembly comes across the hydrophilic outer layer of the cell membrane, the Pluronic micelle can be easily engulfed into the cellular environment. In turn, when the outer micelle layer gets ruptured, the positively charged guanidinium group of L-arginine ligand acts as a handle and electrostatically interacts with the cellular surface at a proper angle to synergize the cellular transfection.

From the XRD pattern (Fig. 1B) it can be observed that dopant ions do not affect the phase purity of the material or induce any strain. The diffraction peaks at 2θ values 30.1, 35.25, 43.15, 53.67, 57.32, and 63.16 correspond to (200), (311), (400), (422), (511) and (440) planes (JCPDS 82-1533), respectively. This pattern is a signature of an inverted spinel structure with the magnetite phase of iron oxide NPs. The particle size of all the samples was calculated by using the Debye–Scherrer formula ($L = 0.9\ \lambda/\beta\cos\theta$) [38], and the FWHM values of the major XRD planes are in the range of 5–12 nm (Table S1). The presence of dopant ions and their amount were studied by energy-dispersive X-ray analysis (EDAX) (Fig. S1). The dopant does not form a new phase, detectable by XRD, which can adversely affect the magnetic property of the material. It is well known that the location of dopant ions in ferrimagnetic inverted spinel material is crucial as it influences the magnetic moment of the material.

In an inverted spinel structure of magnetite, the Fe^{3+} ions present at A sites are anti-ferromagnetically coupled with those present in equal numbers at B sites and cancel the overall magnetism generated due to Fe^{3+} ions. Hence, only Fe^{2+} ions present at B sites are responsible for the observed magnetic property [39]. Now, the dopant ions (in the M^{2+} state) have a preference for the particular interstitial sites which depends on the reaction parameters adopted during the synthesis of the material. Cu^{2+}, Ni^{2+}, and Co^{2+} prefer Oh sites and replace Fe^{2+} ions, resulting in net magnetic moments 1, 2, and 3 μ_B, respectively [40]. This enhanced magnetic moment increases r_2 relaxivity during the MR. Surprisingly, Mn^{2+} and Zn^{2+} ions have a preference for Td sites and the overall magnetic moment is affected by their distribution as well as oxidation state (may be changed during synthesis to Mn^{3+} and Mn^{4+}) [41]. On the contrary, the substitution of Fe^{2+} at the Oh sites by Zn^{2+} ions increases the magnetic moment at lower doses, while the higher doses (> 0.4) favor antiferromagnetic interactions and decrease the magnetic moment [42]. Mössbauer spectroscopy is one of the best techniques to trace the location and to study the local environment around the Fe ions and their interactions. The perturbation in the local environment due to dopants can be very well detected by this technique. The Mössbauer spectroscopy of all the synthesized samples was carried out at RT (300 K), and the results are shown in Table 1. It can be observed that the Fe^{2+}/Fe^{3+} ions in the blank Fe_3O_4 could not couple with each other, confirming the paramagnetic nature. This is due to the spin canting effect predominant at very small particle sizes. On doping Mn^{2+} ions, the hyperfine interaction comes into existence at the A sites, while the Fe ions present at the B sites remain inactive. This is due to Mn^{2+}ions substituting Fe^{2+} at Oh sites perturbing the local environment to make Fe ions couple with each other through oxygen atoms. This results in a hyperfine splitting of energy levels at A sites, while no change in the local environment at B sites. On the contrary, Zn^{2+} ions doping substitutes Fe^{2+}/Fe^{3+} at Oh sites, and in turn, hyperfine splitting can be observed at B sites, while the Fe^{3+}ions at A sites remain silent [43]. Interestingly, Ni^{2+} ions get engaged at both the sites, which results in superexchange interaction among Fe^{3+} ions at Td and Oh sites, while interaction among Fe ions at Oh sites leads to double exchange interaction. These generate sextuplets in Mössbauer spectra [44, 45].

The effect of doping on the magnetic properties of the material was studied by VSM analysis. From the M-H curves (Fig. 2I and Table 1), it can be observed that blank Fe_3O_4 NPs exhibit paramagnetic behavior with less Ms value (30.1 emu/g), while on Zn^{2+}doping, it increases to 72.5 emu/g. Generally, in the bulk form, blank Fe_3O_4 has a Ms value of 80–90 emu/g and it increases upon transforming into a nanoregime [46, 47]. However, the less Ms value, in the present case, indicates surface spin randomness at very small particle size. The enhancement in Ms value on Zn^{2+}doping corroborates the Mössbauer results. On the other hand, Mn^{2+} and Ni^{2+}doping retains the paramagnetic behavior of the material due to the very less particle size [48].

The interaction of L-arginine with Fe_3O_4 NPs surface was studied by FTIR spectroscopy. Free carboxylate ions in acetate form vibrate in two fundamental modes: asymmetric $\nu_{as(COO^-)}$ and symmetric $\nu_{s(COO^-)}$ stretching at 1583

Table 1 Room temperature Mössbauer spectral data of as-synthesized M^{2+}/Fe_3O_4@L-Arg/P NPs

NPs sample	Magnetic field (kOe)		Q.S. in mm/s	I.S mm/sec			Area under curve (%)			Saturation magnetization M_s (emu/g)
	A	B	C	A	B	C	A	B	C	
Fe_3O_4@L-Arg/P	–	–	0.64 (0.02)	–	–	0.36 (0.02)	–	–	1.00	29.8
Ni^{2+}/Fe_3O_4@L-Arg/P	484 (3.2)	428 (3.2)	–	0.39 (0.02)	0.55 (0.02)	0.38 (0.02)	66.3	33.7	–	14.0
Mn^{2+}/Fe_3O_4@L-Arg/P	488 (3.2)	–	0.64 (0.02)	0.17 (0.02)	–	0.33 (0.02)	58.8	–	41.2	8.0
Zn^{2+}/Fe_3O_4@L-Arg/P	–	426.8 (3.2)	0.64 (0.02)	–	0.40 (0.02)	0.32 (0.02)	–	68.4	31.6	72.5

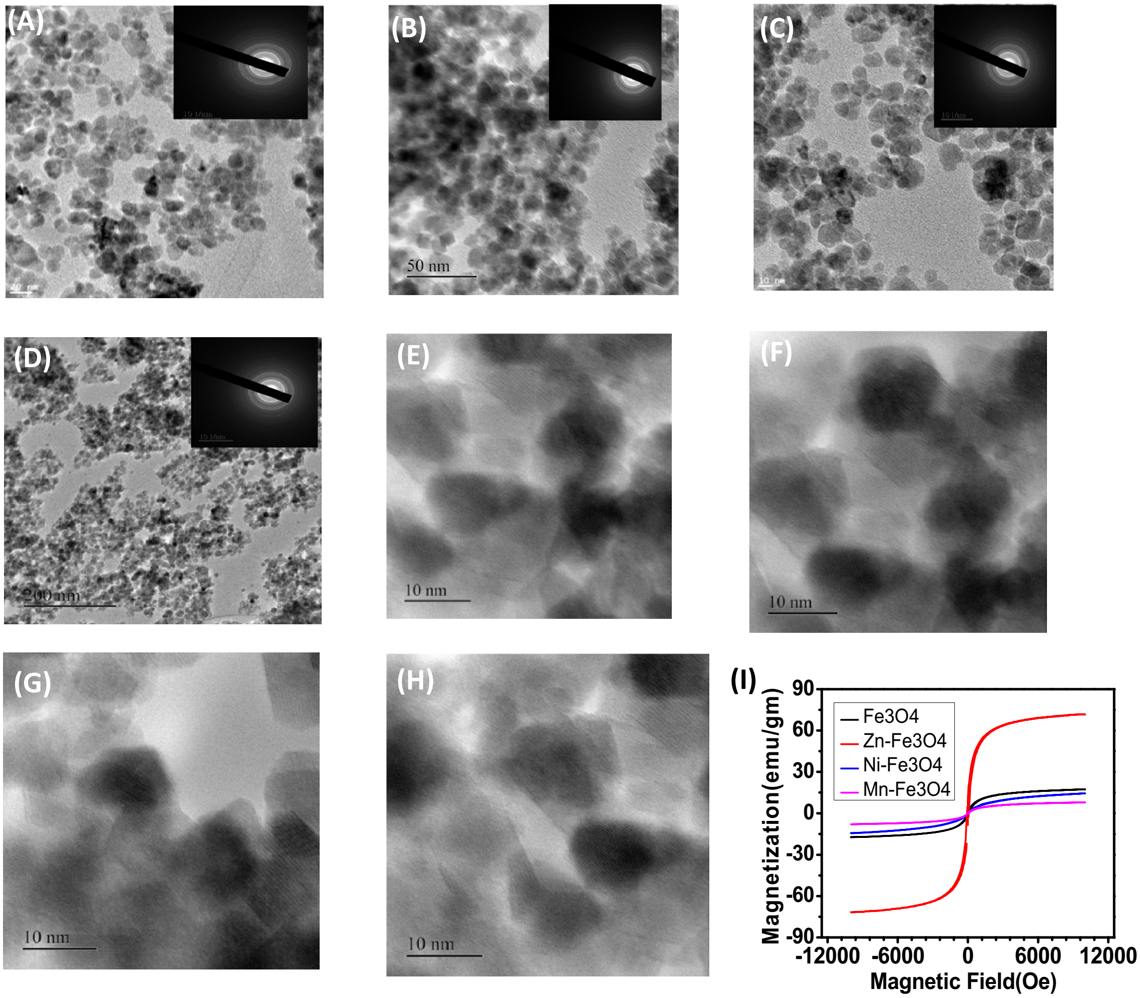

Fig. 2 **A**–**D** HRTEM images (inset image shows SAED pattern) and **E**–**H** lattice fringes at higher magnification of as-synthesized blank, Zn^{2+}, Mn^{2+}, and Ni^{2+}/Fe_3O_4@L-Arg/P NPs, respectively **I** M-H curves

and 1422 cm^{-1}, respectively. In the case of Fe_3O_4@L-arg NPs (Fig. SI 3), the $\nu_{as(COO^-)}$ of carboxylate ions appears at 1645 cm^{-1} and $\nu_{s(COO^-)}$ at 1390 cm^{-1}. Hence, in coordination with surface Fe ions, $\nu_{as(COO^-)}$ increases, while $\nu_{s(COO^-)}$ decreases, indicating monodentate coordination of the carboxylate ion of amino acid. Also, Δ ($\nu_{as(COO^-)} - \nu_{s(COO^-)}$) < Δ' ($\nu'_{as(COO^-)} - \nu'_{s(COO^-)}$), where Δ is the difference in the absorption bands for free carboxylate ions and Δ' for metal-bound carboxylate ions, suggesting monodentate coordination [49–51]. The absorption at 646 cm^{-1} corresponds to Fe–O stretching in the Fe_3O_4 inverse spinel system. Absorptions at 1111 and 1156 cm^{-1} are due to the presence of the block copolymer completely encapsulating the NPs surface and –CH_2-rocking vibration of Pluronic, respectively [52]. Moreover, the successful encapsulation of NPs surfaces by the Pluronic-F127 layer was also confirmed by the thermal analyses (discussed in detail later). Further, the size and shape of M^{2+}/Fe_3O_4@L-Arg/P NPs were studied by High-Resolution Transmission Electron Microscopy (HRTEM) analysis. The HRTEM images show spherical particles, and the size histograms reveal 10–12 nm particle size. The SAED patterns show the polycrystalline nature of the material (Fig. 2).

Phantom study

The efficiency of the CAs depends upon their ability to shorten the relaxation time of the protons in the vicinity. Under the influence of an applied magnetic field, the excited protons having spins parallel to the field resonantly absorb the electromagnetic energy irradiated by radio waves. This results in the spins being anti-parallel to the field. These high-energy spins relax back to the original state on the removal of the radio waves through two relaxation processes: (i) longitudinal relaxation indicated by relaxation time T_1 required to recover 63% magnetization of the equilibrium value and (ii) transverse relaxation expressed by time T_2 required to drop the 37% magnetization of its initial magnitude. These relaxation processes directly affect the MRI signal intensity, and as per definition, T_1 enhances the signal intensity, while T_2 diminishes the same, and CA present in the vicinity of the protons perturbs these processes referred to as positive or negative contrast agents, respectively. Hence, positive CAs shorten the T_1 which makes the signal recovery fast which in turn enhances the signal intensity producing a bright image. Negative CAs shorten the T_2 of the protons by dropping the transverse magnetization quickly resulting in a loss of signal intensity and creating a dark image [6, 53]. The efficiency with which the CA enhances the proton relaxation rate of water is referred to as relaxivity (r). The r_1/r_2 ratio is used as a marker to decide whether the CAs work as a positive or a negative. Good T_1 CAs have r_2/r_1 less than 5, and T_2 CAs have a high r_2/r_1 ratio (> 10) [5]. The correlation between T_1 and T_2 relaxation rates (R_1 or R_2) and the concentration of CAs can be investigated through the phantom study. The sequences of the radio frequency signal repetition time (TR) and the detection or echo time (TE) were designed such that the T_1-weighted and T_2-weighted images of the cross section of a capillary containing the sample in a coronal mode can be captured in an MRI machine [54]. It can be observed from Fig. 3 that the relaxation rates vary linearly with the concentration of NPs. The longitudinal relaxivity (r_1) or transverse relaxivity (r_2) was calculated from the slope of the lines and is reported in Table 2. It can be observed that blank Fe_3O_4@L-Arg NPs can generate bright contrast, contrary to their inherent nature of producing a dark image. This is due to the very small particle size as explained earlier. On Zn^{2+}doping, there is a small decrease in r_1 values compared to blank Fe_3O_4, while that of r_2 increases drastically increasing the r_2/r_1 ratio, which qualifies the material to act as a T_2 CA. This result is in correlation with Mössbauer and VSM studies. On doping Zn^{2+}ions, the Ms value drastically increased resulting in a superparamagnetic material. This effect is due to replacing Fe^{3+} ions present at the Td sites in an inverted spinel structure. As a consequence, there is a decrease in antiferromagnetic communication among the Fe^{3+} ions at the Td and Oh sites which cannot cancel out the spin completely, resulting in the enhancement of Ms [55]. On doping with Mn^{2+}, the r_2 relaxivity increases from 21.5 to 32.4; however, that of r_1 also increases from 5.37 to 6.05 producing a low r_2/r_1 ratio, enabling the material to act as T_1 CA. The M-H plot also corroborates this result showing paramagnetic behavior with very small particle size. It has been observed that Mn^{2+} has a preference for both Td and Oh sites resulting in a mixed spinel structure. In the present case, it is confirmed from the Mössbauer spectroscopy that Mn^{2+} ions substitute Fe^{2+} from Oh sites, feeding the unpaired electrons in the sites, which results in enhanced communication among the electronic

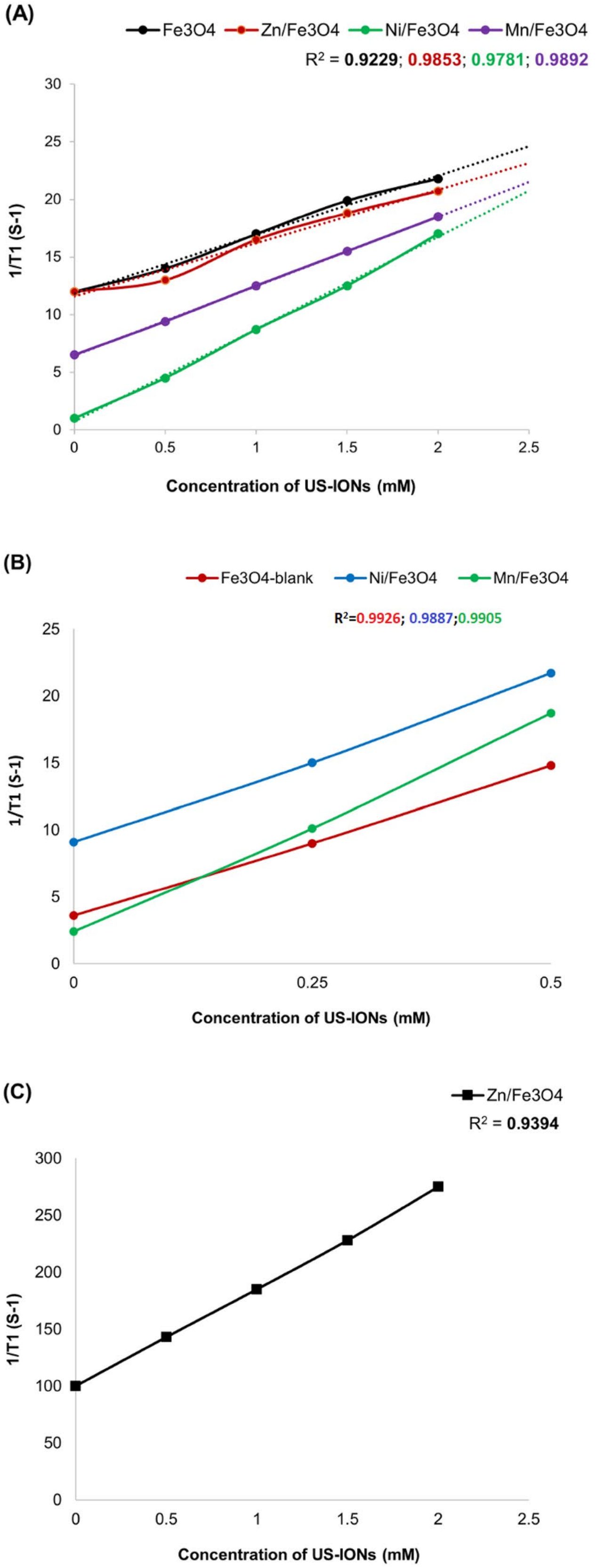

Fig. 3 **A** $1/T_1$ **B** and **C** $1/T_2$ Vs concentration of M^{2+}/Fe_3O_4@L-Arg/P NPs

Table 2 Longitudinal and transverse relaxivities and their ratio of as-synthesized M^{2+}/Fe_3O_4@L-Arg/P NPs

Sample	r_2 ($mM^{-1}\ s^{-1}$)	r_1 ($mM^{-1}\ s^{-1}$)	r_2/r_1
Fe_3O_4@L-Arg/P	21.49	5.27	4.079
Zn^{2+}/Fe_3O_4@L-Arg/P	86.57	4.52	19.17
Ni^{2+}/Fe_3O_4@L-Arg/P	24.36	7.70	3.16
Mn^{2+}/Fe_3O_4@L-Arg/P	32.40	6.05	5.35

spins resulting in a rise in r_2 relaxivity. This substitution of ions also synergistically reduces the proton relaxation time to recover the longitudinal magnetization, thereby increasing the r_1 [56]. On doping with Ni^{2+} replaces Fe^{3+} and Fe^{2+}/Fe^{3+} from Td and Oh sites facilitate the electronic spins to couple ferromagnetically and enhance the Ms. However, in the present case, both r_1 and r_2 relaxivities increase giving rise to low relaxivity ratio. Hence, doping with Ni^{2+} in USION synergistically enhances the recovery of longitudinal magnetization and enables the material to act as a T_1 CA (Tables 3 and 4).

It can be observed from Tables 3 and 4 that blank Fe_3O_4@L-Arg/P NPs produce bright images at very low concentrations (0.001 mM) and doping Ni^{2+} synergistically brightens the image at this low concentration. This effect is continued up to 0.1 mM. Then the image gets distorted at higher concentrations (0.25 and 0.5 mM). In the case of Zn^{2+}/Fe_3O_4@L-Arg/P NPs, the T_2 contrasting effect is achieved at 0.1 mM, while higher concentrations (0.25 and 0.5 mM) are not effective in producing a dark image. No contrasting effect was produced in the case of Mn^{2+}/Fe_3O_4@L-Arg/P at a low concentration range. This material produces a T_1 contrast effect at 0.5 mM.

Discussion

The commercially available Gd-DTPA and Gd-DOTA complexes have their ninth valence satisfied by a water molecule ($q=1$). There is a very small energy difference between their eighth and ninth valence. Hence, the ninth coordinated water ligand is labile and continuously gets exchanged with bulk water molecules [57]. This process is dynamic. Due to this, the molecular tumbling increases. These commercial CAs have one coordinated water molecule ($q=1$); however, the complexes with $q=2$, 3, and 4 have also been developed to increase the r_1 relaxivity of bulk water protons in an applied field which, in turn, enhances the T_1 contrasting. The efficiency of T_1 CAs depends on three parameters (Eq. 5)

$$\left(\frac{1}{T_1}\right)=q.P_m\left[\frac{1}{\left(T_{1m}+\tau_M\right)}\right] \tag{5}$$

Table 3 T_2-weighted ($TR=3000/TE=98.8$ ms) MR images for different concentrations of M^{2+}/Fe_3O_4@L-Arg/P NPs systems

Sr. No.	Sample	Concentration (mM)					
		0.5	0.25	0.1	0.05	0.01	0.001
1	Fe_3O_4@L-arg/P						
2	Zn^{2+}/Fe_3O_4@L-arg/P		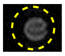				
3	Ni^{2+}/Fe_3O_4@L-arg/P						
4	Mn^{2+}/Fe_3O_4@L-arg/P						

Table 4 T_1-weighted ($TR=800/TE=11.5$ ms) MR images for different concentrations of M^{2+}/Fe_3O_4@L-Arg/P NPs.

Sr. No	Sample	Concentration (mM)					
		0.5	0.25	0.1	0.05	0.01	0.001
1	Fe_3O_4@L-Arg/P		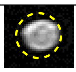				
2	Zn^{2+}/Fe_3O_4@L-Arg/P		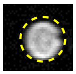				
3	Ni^{2+}/Fe_3O_4@L-Arg/P						
4	Mn^{2+}/Fe_3O_4@L-Arg/P						

where T_{1m} is the longitudinal relaxation time of the inner-sphere bounded water protons, q is the number of coordinated water molecules in the first coordination sphere, P_m is the mole fraction of water coordinated to the metal center (in the case of Gd complexes), and τ_M is the mean water residence time near the metal center. If the value of τ_M is very small, then it results in only ($1/T_{1\mathrm{m}}$), the relaxation rate of inner-sphere water. Hence, a high relaxation rate depends on a higher value of q. The SBM theory for paramagnetic relaxation suggests that optimization of correlation time (τ_c) is essential to obtain higher relaxivity (Eq. 6) [58]

$$\left(\frac{1}{\tau_{ci}}\right) = \left(\frac{1}{\tau_M}\right) + \left(\frac{1}{\tau_R}\right) + \left(\frac{1}{T_{ie}}\right) \quad i = 1, 2 \tag{6}$$

The Gd-DTPA chemistry for proton relaxivity to produce bright MR images is well established and predicted by SBM theory [59, 60]. However, to avoid the problems concerning free Gd leaching and consequent complications due to toxicity, the development and application of iron oxide-based MRI CAs having the capability to induce longitudinal relaxation of water protons (for brighter images) need focused attention. The H-bonding can arrange the water molecules in a definite order, and its strength can be modulated by varying the donor hetero atoms and acceptor H atoms present in the ligand. These molecules can in turn be compacted by an outer polymeric surfactant micelle. This strategy can control the molecular tumbling (τ_R) of the water molecules. From a three-dimensional perspective, there can also be a faster water exchange between these surface-ligand-bound H-bonded water molecules and those of the bulk water molecules through diffusion. In this way, the τ_M parameter can be controlled. The advantage of this strategy is that the number of inner spheres water molecules (q) will be more than one and this high number will collectively make the electronic relaxation time (T_{ie}) longer. Overall, high proton relaxivity can be achieved by tuning both the core and the shell environment in the developed USIONs (Scheme 2).

It can be observed from Table 2 that blank Fe_3O_4@L-Arg/P NPs show 5.27 $\mathrm{mM}^{-1}\ \mathrm{s}^{-1}$ r_1 relaxivity, while the commercial Gd-DTPA complex has an r_1 value of ca. 4 $\mathrm{mM}^{-1}\ \mathrm{s}^{-1}$ and that of Ferridex® has ca. 10 $\mathrm{mM}^{-1}\ \mathrm{s}^{-1}$ (used as T_2 CAs due to its very high r_2 value). Hyeon group studied T_1 contrast enhancement in extremely small iron oxide NPs (ESIONs) having 2.2, 3, and 12 nm diameter and the observed r_1 values 4.78, 4.77, and 2.37 $\mathrm{mM}^{-1}\ \mathrm{s}^{-1}$, respectively [24]. In the present case, Zn^{2+}/Fe_3O_4@L-Arg/P NPs show almost a similar value (4.52 $\mathrm{mM}^{-1}\ \mathrm{s}^{-1}$), while blank, Ni^{2+}, and Mn^{2+}-doped Fe_3O_4@L-Arg/P show a gradual increase in r_1 up to 7.70 $\mathrm{mM}^{-1}\ \mathrm{s}^{-1}$. These results indicate that H-bonded inner sphere water molecules can increase the r_1 relaxivity up to ca. 3–4 $\mathrm{mM}^{-1}\ \mathrm{s}^{-1}$. To evaluate the presence of inner sphere H-bonded water in the shell environment, a thermal analysis of all the samples was carried out (Fig. 4). It can be observed from the thermograms that all the samples except Zn^{2+}/Fe_3O_4@L-Arg/P exhibit two kinds of weight loss in the range of 50–85 and around 150 °C due to bulk and interior surface-bound water, respectively. The weight loss above 100 °C is continued and persisted till 150 °C, confirming the presence of inner sphere H-bonded water. The weight losses at higher temperatures are due to the carbonization of organic material, confirming the presence of a pluronic layer at the outer shell. Hence, it can be claimed that the r_1 relaxivity of the bulk water protons can be raised by H-bonded water molecules present near the core of magnetic NPs.

In vitro drug release kinetics, cell viability, and cytotoxicity studies

The M^{2+}/Fe_3O_4@L-Arg/P NPs were tested as drug delivery vehicles for the epidermoid carcinoma cell line A431 to evaluate the anti-cancer activity of the loaded drug (Brigatinib). The smooth release, cytotoxicity, and colony-forming ability of these formulations were checked by the drug release kinetics, MTT, and clonogenic assays, respectively. A wide range of doses as described in the individual experiments were used to make a comparison among the formulations (M^{2+}/Fe_3O_4@L-Arg/P/bg).

The kinetics of in vitro release of brigatinib from M^{2+}/Fe_3O_4@L-Arg/P (Fig. 5) was studied in PBS solution at 7.4 pH. It can be observed that Mn^{2+}/Fe_3O_4@L-Arg/P/bg USIONs showed fast initial release as compared to those of Ni^{2+}-doped. Mn^{2+}/Fe_3O_4@L-Arg/P/bg USIONs release 30% of the drug in a first burst in 5 h and the next 20% release in 72 h with an overall 50% release in three days. Approximately 70% drug was released from Ni^{2+}/Fe_3O_4@L-Arg/P/bg in three days. The Mn^{2+}/Fe_3O_4@L-Arg/P/bg USIONs started to release the drug early and, however, took a long time to reach the 70% release rate than Zn^{2+} and Ni^{2+}-doped vehicles. From this release kinetics study, it can be said that the release efficiency of the delivery vehicle is modulated by varying the dopant ions. This might be due to the restructuring of the surface. The defect produced due to the mismatch of the atomic radius of the dopant and host responsible for the physical interaction of the surface with the ligand and the drug molecules, in turn, affects the smooth release of the drug.

The cytotoxic effect of the synthesized USIONs with or without the drug was studied by MTT assay, on the A431 human epidermoid carcinoma cell line (Fig. S3). The bare drug remains inactive toward cell viability at microgram-level dosage. However, the drug-loaded USIONs (M^{2+}/Fe_3O_4@L-Arg/P) affect it at the same level of dosage. M^{2+}/Fe_3O_4@L-Arg/P/bg USIONs with 10 µg/mL dose can reduce the cell viability to 53, 31, and 94 for Zn^{2+}, Mn^{2+},

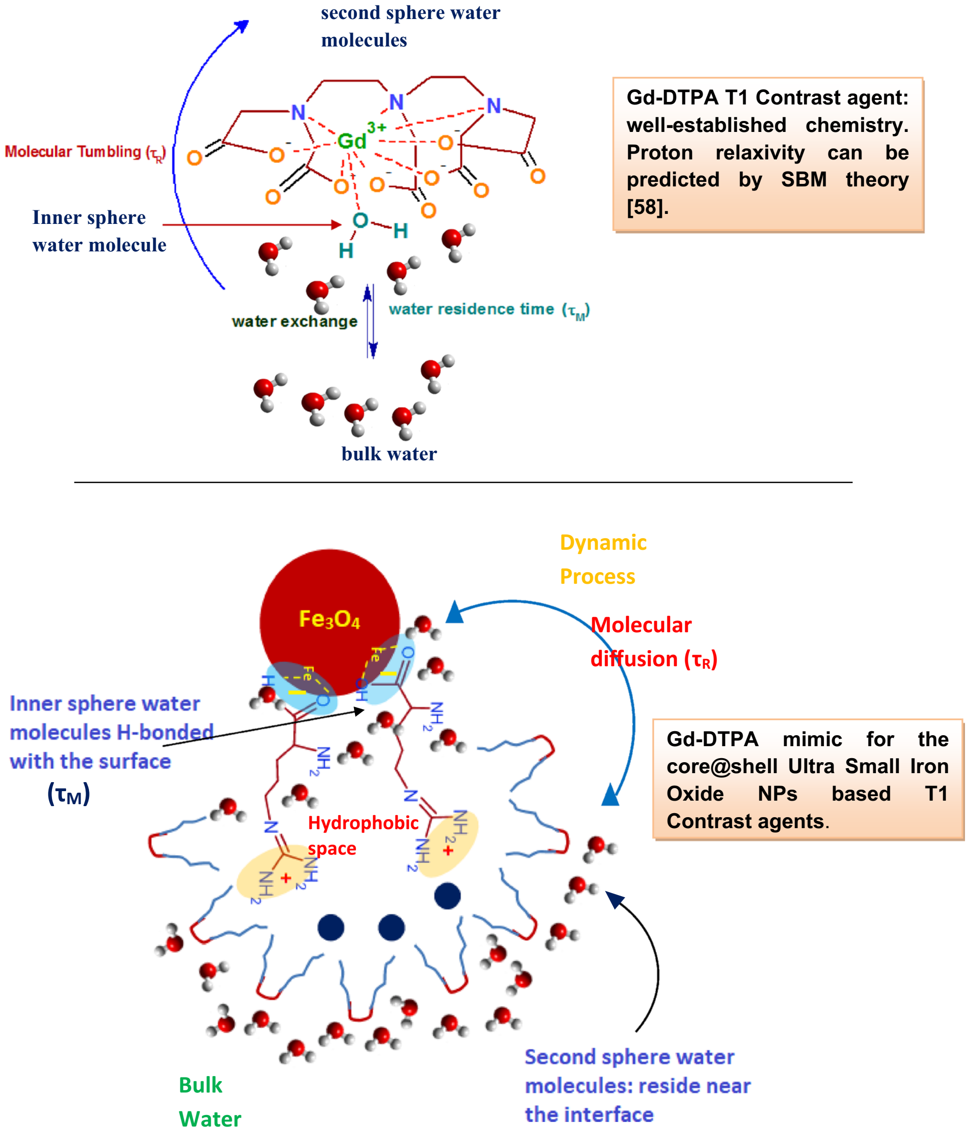

Gd-DTPA T1 Contrast agent: well-established chemistry. Proton relaxivity can be predicted by SBM theory [58].

Gd-DTPA mimic for the core@shell Ultra Small Iron Oxide NPs based T1 Contrast agents.

Scheme 2 The upper panel shows standard Gd-DTPA chemistry from SBM theory. The lower panel shows the proposed Gd-DTPA mimic based on the proposed tuning of the core@shell environment of USIONs

and Ni^{2+}, respectively. In the case of the blank carrier (Fe$_3$O$_4$@L-Arg/P), the % cell viability remains basal even at higher dosages emphasizing the safety of the developed delivery platforms. Mn^{2+}/Fe$_3$O$_4$@L-Arg/P/bg boosts the significant cell death at very low dosage levels as compared to Zn^{2+}/Fe$_3$O$_4$@L-Arg/P/bg system (Fig. S3B and S3D), while Ni^{2+}/Fe$_3$O$_4$@L-Arg/P/bg NPs induce the cell death at very high concentration (1000 µg/mL) and does not reduce the cell numbers even if it can release the drug easily (Fig. S3C).

The in vitro cell survival assay is based on the ability of a single cell to grow into a colony. It is generally carried out to determine the effect of a drug on the proliferation of tumor cells. The MTT assay demonstrated the high efficiency of the formulations as compared to the bare drug. It sheds light on the ability of the formulations to prevent colony formation often exhibited by cancer tumor cells. It can be observed from Fig. 6B and D that only 50% of colonies survived in the case of Zn^{2+}/Fe$_3$O$_4$@L-Arg/P/bg and Mn^{2+}/Fe$_3$O$_4$@L-Arg/P/bg at about 50 µg/mL dosage, while Ni^{2+}/Fe$_3$O$_4$@L-arg/P/bg did not cause any reduction in colony number at that concentration (Fig. 6C). These results indicate that Ni^{2+}/Fe$_3$O$_4$@L-Arg/P/bg can act as good delivery vehicle as compared to the other developed vehicles.

Hence, the present study emphasizes that the efficiency of the vehicle to release the drug is its integral property and is influenced by the factors like the surface-ligand binding strength, the surrounding environment of the entrapped drug molecules, and the perturbance of the core's magnetism by dopant ions, etc. It would be interesting to carry out in vivo studies regarding drug delivery and MR imaging, which will be the focus of our next study.

]

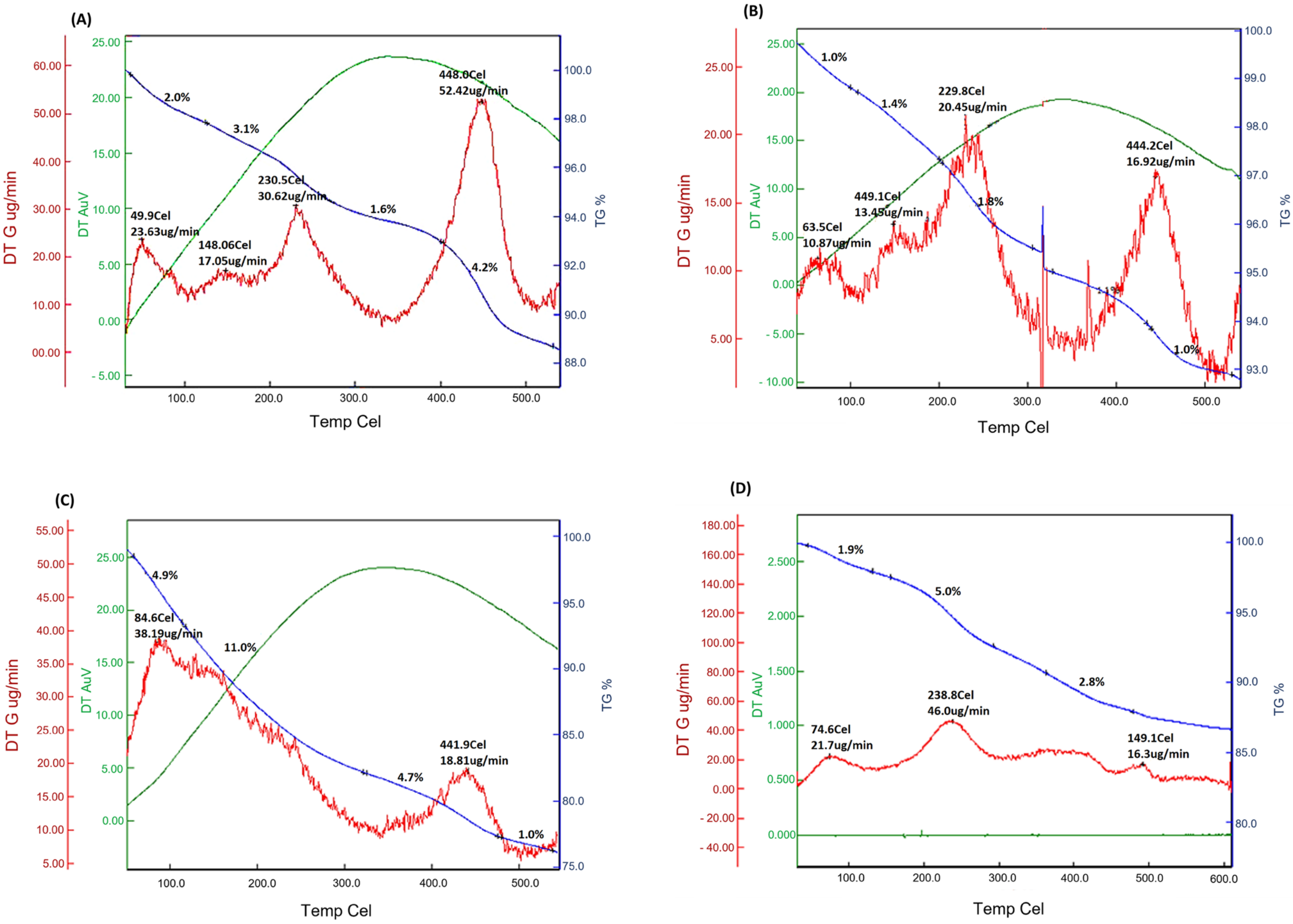

Fig. 4 Thermal analysis of **A** Fe_3O_4@L-Arg/P, **B** Ni^{2+}/Fe_3O_4@L-Arg/P, **C** Mn^{2+}/Fe_3O_4@L-Arg/P, and **D** Zn^{2+}/Fe_3O_4@L-Arg/P NPs

Fig. 5 Percentage release of brigatinib from blank, Zn^{2+}, Mn^{2+}, and Ni^{2+}-doped Fe_3O_4@L-Arg/P/bg. The drug released from Mn^{2+}-doped Fe_3O_4@L-Arg/P/bg is the earliest as compared to others. However, at the end of three days (72 h), more drug is released from Zn^{2+} and Ni^{2+}-doped USIONs than Mn^{2+}-doped ones

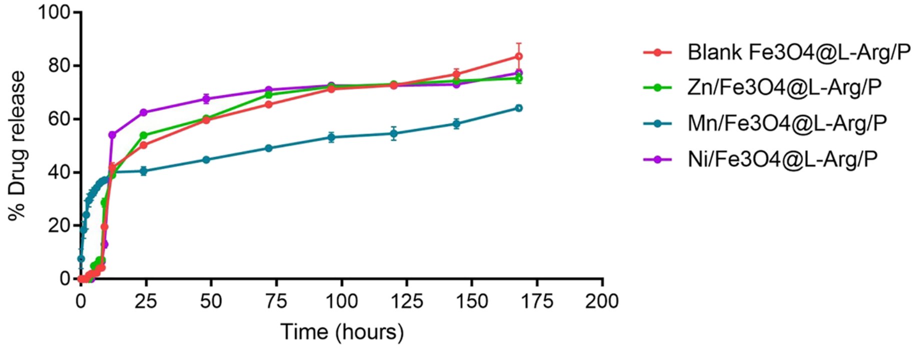

Conclusion

Small amino acid molecules like L-arginine can act as capping and chelating ligands to bind Fe_3O_4 nanoparticles tightly, restrict their growth at the nanoregime, and form USIONs. Pluronic F127 encapsulates L-Arg-capped USIONs effectively and forms polymeric micelles while retaining magnetic properties. The synthesized Pluronic-encapsulated and L-Arg-capped Fe_3O_4 magnetic micelles can act as drug delivery platforms to load the hydrophobic anti-cancer drug brigatinib in their hydrophobic shells. Blank, Mn^{2+}, and Ni^{2+}-doped Fe_3O_4@L-Arg NPs reveal T_1 contrasting ability while those of Zn^{2+}-doped NPs show T_2 contrasting due to the modification in relaxivity ratio. Out of these, Ni^{2+}-doped USIONs are the best T_1 CAs. The drug-loaded Ni^{2+}/Fe_3O_4@L-Arg/P/bg exhibits good drug release kinetics. But the MTT

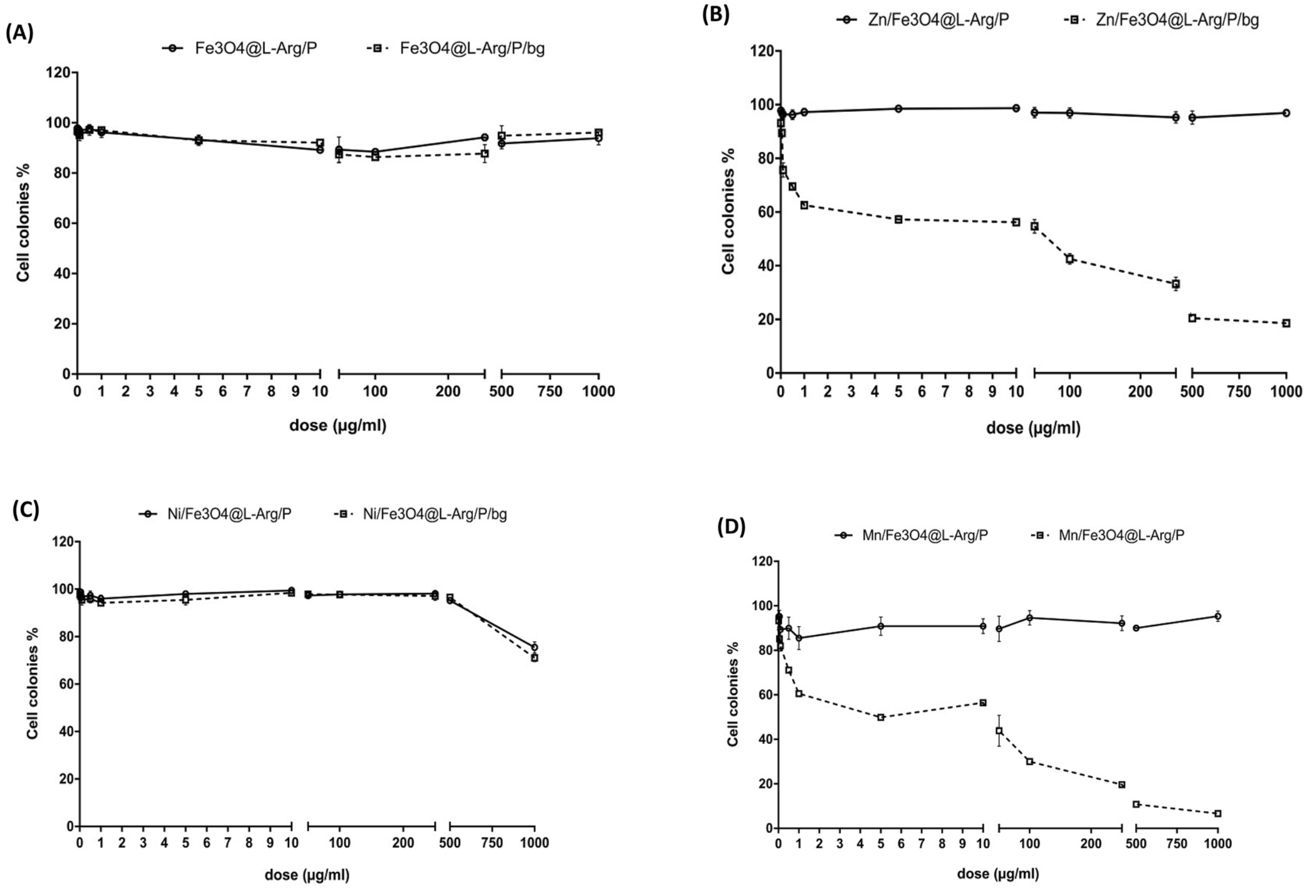

Fig. 6 Clonogenic assay: **A** No visible change in the plates was observed in presence of the bared drug at any concentration (in µg level). The number of colonies remained constant throughout **B** colony formation was reduced early at 1 µg mL^{-1} of the Zn^{2+}/Fe$_3$O$_4$@L-Arg/P/bg. Only a handful of colonies were observed at 500 to 1000 µg mL^{-1} of formulation. **C** No change in the number of colonies on the addition of Ni^{2+}/Fe$_3$O$_4$@L-Arg/P/bg. The reduction in the number of colonies observed above 500 µg mL^{-1} dose. **D** The colony formation drastically decreased at 1 µg mL^{-1} dose of Mn^{2+}/Fe$_3$O$_4$@L-Arg/P/bg formulation. The number of colonies continues to decrease due to an increase in cell death

assay suggests the need for a higher dosage to produce a pronounced effect. In this context, Mn^{2+}-doped vehicles are more efficient. Only a very low dosage is required for cell death, and it is also true for clonogenic assay. In vitro cellular uptake of drug-loaded magnetic micelles by epidermoid carcinoma cell line (A431) shows more internalization than the bare drug. The overall size of the drug-loaded magnetic micelles allowed prolonged circulation and sustained drug delivery. Toxicity studies confirm the safety of the developed iron oxide nanoparticle-based magnetic micelles as drug delivery vehicles at a dosage range of 0.125–0.25 mg/mL. Rationally, it can be claimed that Mn^{2+}-doped USIONs are very suitable for theranostic applications. This study leaves some questions unanswered like (1) how do dopant ions and consequent modification in the magnetic property of the core (by maintaining the shell environment constant) affect the drug release kinetics and proliferation of tumor cells? (2) Can the strength of the H-bonds among surface-bound ligands and water molecules in the shell environment be evaluated to study the proton relaxivity of bulk water? (3) Can the contrasting ability of the MRI CAs be modulated by varying only the shell environment and keeping the core/core size constant? Further research is required to answer these questions.

Supplementary Information The online version contains supplementary material available at https://doi.org/10.1007/s13738-023-02781-2.

Acknowledgements SDM thanks Science & Engineering Research Board (SERB), New Delhi, India, for appointing as SERB-National Post-Doctoral Fellow (No. PDF/2017/002272) under the mentorship of HPS. HPS thanks the Science & Engineering Research Board (SERB), New Delhi, India, for financial support under a sponsored scheme (No. EMR/2016/007638). SkR and KG thank Nanomission, Department of Science & Technology, India, for financial support (No. SR/NM/NS-91/2016). We also thank Prof. A. V. Ramachandran for the necessary suggestions and corrections in the manuscript.

Authors' contribution BS contributed to data curation, formal analysis, methodology, investigation, software. SDM helped in data curation, formal analysis, methodology, funding acquisition, project administration, writing original draft. UV contributed to data curation, formal analysis, methodology, investigation (biological part). SB helped in conceptualization, validation, writing & editing (biological part). SkR contributed to data curation and formal analysis. KG helped in conceptualization, microscopic, and magnetic analyses, validation. MS contributed to validation, Mössbauer spectroscopy, data curation, and HPS contributed to conceptualization, funding acquisition, project administration, resources, visualization, validation, final writing, reviewing & editing.

Declarations

Conflict of interest There are no conflicts to declare.

References

1. W. Wei, C.Z. Jiang, V.A.L. Roy, Nanoscale **8**, 19421 (2016). https://doi.org/10.1039/C6NR07542H
2. E.-K. Lim, T. Kim, S. Paik, S. Haam, Y.-M. Huh, K. Lee, Chem. Rev. **115**, 327 (2015). https://doi.org/10.1021/cr300213b
3. Z.R. Lu, P. Qiao, Mol. Pharm. **15**, 3603 (2018). https://doi.org/10.1021/acs.molpharmaceut.8b00037
4. M.U. Muckenthaler, S. Rivella, M.W. Hentze, B. Galy, Cell **168**, 344–361 (2017). https://doi.org/10.1016/j.cell.2016.12.034
5. N. Lee, T. Hyeon, Chem. Soc. Rev. **41**, 2575 (2012). https://doi.org/10.1039/C1CS15248C
6. R.C. O'Handley, *Modern magnetic materials: principles and applications* (Wiley-Interscience, Hoboken, 1999)
7. J.W.M. Bulte, D.L. Kraitchman, NMR Biomed. **17**, 484 (2004). https://doi.org/10.1002/nbm.924
8. B.D. Cullity, *Introduction to magnetic materials* (Addision Wesley, Boston, 1972)
9. Q.A. Pankhurst, J. Connolly, S.K. Jones, J. Dobson, J. Phys. D: Appl. Phys. **36**, 167 (2003). https://doi.org/10.1088/0022-3727/36/13/201
10. U. Jeong, X. Teng, Y. Wang, H. Yang, Y. Xia, Adv. Mater. **19**, 33 (2007). https://doi.org/10.1002/adma.200600674
11. Y.S. Kang, S. Risbud, J.F. Rabolt, P. Stroeve, Chem. Mater. **8**, 2209 (1996). https://doi.org/10.1021/cm960157j
12. X.K. Zhao, P.J. Horve, J.H. Fendler, J. Phys. Chem. **93**, 908 (1989). https://doi.org/10.1021/j100339a070
13. Y.-X.J. Wang, Quant. Imaging Med. Surg. **1**, 35 (2011). https://doi.org/10.3978/j.issn.2223-4292.2011.08.03
14. F. Kiessling, M.E. Mertens, J. Grimm, T. Lammers, Radiology **273**, 10 (2014). https://doi.org/10.1148/radiol.14131520
15. L. Sandiford, A. Phinikaridou, A. Protti, L.K. Meszaros, X.J. Cui, Y. Yan, G. Frodsham, P.A. Williamson, N. Gaddum, R.M. Bottnar, P.J. Blower, M.A. Green, T.M. de Rosales, ACS Nano **7**, 500 (2013). https://doi.org/10.1021/nn3046055
16. A. Cabrera-Garcia, E. Checa-Chavarria, J. Pacheco-Torres, A. BernabeuSanz, A. Vidal-Moya, E. Rivero-Buceta, G. Sastre, E. Fernandez, P. Botella, Nanoscale **10**, 6349 (2018). https://doi.org/10.1039/C7NR07948F
17. C. Tu, E.A. Osborne, A.Y. Louie, Ann. Biomed. Eng. **39**, 1335 (2011). https://doi.org/10.1007/s10439-011-0270-0
18. A. Senpan, S.D. Caruthers, I. Rhee, N.A. Mauro, D. Pan, G. Hu, M.J. Scott, R.W. Fuhrhop, P.J. Gaffney, S.A. Wickline, G.M. Lanza, ACS Nano **3**, 3917 (2009). https://doi.org/10.1021/nn900819y
19. J. Wahsner, E.M. Gale, A. Rodríguez-Rodríguez, P. Caravan, Chem. Rev. **119**, 957 (2019). https://doi.org/10.1021/acs.chemrev.8b00363
20. E.A. Schellenberger, A. Bogdanov Jr., D. Hogemann, J. Tait, R. Weissleder, L. Josephson, Mol. Imaging **1**, 102 (2002). https://doi.org/10.1162/15353500200202103
21. T. Hyeon, Chem. Commun. **8**, 927 (2003). https://doi.org/10.1039/B207789B
22. X. Wang, R.D. Tilley, J.J. Watkins, Langmuir **30**, 1514 (2014). https://doi.org/10.1021/la404757q
23. N. Lee, D. Yoo, D. Ling, M.H. Cho, T. Hyeon, J. Cheon, Chem. Rev. **115**, 10637 (2015). https://doi.org/10.1021/acs.chemrev.5b00112
24. B.H. Kim, N. Lee, H. Kim, K. An, Y.I. Park, Y. Choi, K. Shin, Y. Lee, S.G. Kwon, H.B. Na, J.G. Park, T.Y. Ahn, Y.W. Kim, W.K. Moon, S.H. Choi, T. Hyeon, J. Am. Chem. Soc. **133**, 12624 (2011). https://doi.org/10.1021/ja203340u
25. S.H. Lee, B.H. Kim, H.B. Na, T. Hyeon, Nanomed. Nanobiotechnol. **6**, 196 (2013). https://doi.org/10.1002/wnan.1243
26. F.L. Deepak, M. Bañobre-López, E. Carbó-Argibay, M.F. Cerqueira, Y. Piñeiro Redondo, J. Rivas, C.M. Thompson, S. Kamali, C. Rodríguez-Abreu, K. Kovnir, Y.V. Kolen'ko, J. Phys. Chem. C. **119**, 11947 (2015). https://doi.org/10.1021/acs.jpcc.5b01575
27. D.A. Benaron, Cancer Metastasis Rev. **21**, 45 (2002). https://doi.org/10.1023/A:1020131208786
28. S. Bedi, S.A. Khan, M.M. AbuKhader, P. Alam, N.A. Siddiqui, A.A. Husain, Saudi Pharm. J. **26**, 755 (2018). https://doi.org/10.1016/j.jsps.2018.04.010
29. M.D. Vincent, M.S. Kuruvilla, N.B. Leighl, S. Kamel-Reid, Curr. Oncol. **19**, 33 (2012). https://doi.org/10.3747/co.19.1149
30. C.M. Della Corte, G. Viscardi, R.D. Liello, M. Fasano, E. Martinelli, T. Troiani, F. Ciardiello, F. Morgillo, Mol. Cancer **17**, 30 (2018). https://doi.org/10.1186/s12943-018-0776-2
31. W.S. Huang, S. Liu, D. Zou, M. Thomas, Y. Wang, T. Zhou, J. Romero, A. Kohlmann, F. Li, J. Qi, L. Cai, T.A. Dwight, Y. Xu, R. Xu, R. Dodd, A. Toms, L. Parillon, X. Lu, R. Anjum, S. Zhang, F. Wang, J. Keats, S.D. Wardwell, Y. Ning, Q. Xu, L.E. Moran, Q.K. Mohemmad, H.G. Jang, T. Clackson, N.I. Narasimhan, V.M. Rivera, X. Zhu, D. Dalgarno, W.C. Shakespeare, J. Med. Chem. **59**, 4948 (2016). https://doi.org/10.1021/acs.jmedchem.6b00306
32. E. Shah, A. Kadam, T. Jubin, R. Begum, P. Upadhyay, H.P. Soni, ChemistrySelect **4**, 7883 (2019). https://doi.org/10.1002/slct.201900964
33. E. Shah, P. Upadhyay, M. Singh, M.S. Mansuri, R. Begum, N. Sheth, H.P. Soni, New J. Chem. **40**, 9507 (2016). https://doi.org/10.1002/slct.201900964
34. P.R. Desai, N.J. Jain, R.K. Sharma, P. Bahadur, Colloids Surf. A. **178**, 57 (2001). https://doi.org/10.1016/S0927-7757(00)00493-3
35. M.J. Rosen, X.Y. Hua, J. Colloid Interface Sci. **86**, 164 (1982). https://doi.org/10.1016/0021-9797(82)90052-2
36. Y.C. Luiking, G.A.M.T. Have, R.R. Wolfe, N.E.P. Deutz, Am. J. Physiol. Endocrinol. Metab. **303**, E1177 (2012). https://doi.org/10.1152/ajpendo.00284.2012
37. S. Kerkhofs, T. Willhammar, H.V.D. Noortgate, C.E.A. Kirschhock, E. Breynaert, G.V. Tendeloo, S. Bals, J.A. Martens, Chem. Mater. **27**, 5161 (2015). https://doi.org/10.1021/acs.chemmater.5b01772
38. R. Jenkins, R.L. Snyder, *Introduction to X-ray powder diffractometry* (John Wiley & Sons, Hoboken, 1996)
39. M.L. Neel, Ann. Phys. **12**, 137 (1948). https://doi.org/10.1051/anphys/194812030137
40. J.H. Lee, Y.M. Huh, Y.W. Jun, J.W. Seo, J.T. Jang, H.T. Song, S. Kim, E.J. Cho, H.G. Yoon, J.S. Suh, J. Cheon, Nat. Med. **13**, 95 (2007). https://doi.org/10.1038/nm1467
41. R.A. McCurrie, *Ferromagnetic materials: structure and properties* (Academic Press, Cambridge, 1994)

42. J.T. Jang, H. Nah, J.H. Lee, S.H. Moon, M.G. Kim, J. Cheon, Angew. Chem. Int. Ed. **48**, 1234 (2009). https://doi.org/10.1002/anie.200805149
43. J. Liu, Y. Bin, M. Matsuo, J. Phys. Chem. C. **116**, 134 (2012). https://doi.org/10.1021/jp207354s
44. F. Grasset, N. Labhsetwar, D. Li, D.C. Park, N. Saito, H. Haneda, O. Cador, T. Roisnel, S. Mornet, E. Duguet, J. Portier, J. Etourneau, Langmuir **18**, 8209 (2002). https://doi.org/10.1021/la020322b
45. S.M. Kamali, A.M. Blixt, L. Haggstrom, R. Wappling, V. Stanciu, P. Nordblad, J. Magn. Magn. Mater. **272**, 1263 (2004). https://doi.org/10.1016/j.jmmm.2003.12.095
46. K.M. Krishnan, IEEE Trans. Magn. **46**, 2523 (2010). https://doi.org/10.1109/TMAG.2010.2046907
47. U. Schwertmann, R.M. Cornel, *The Iron Oxides* (Wiley-VCH, Weinheim, 2000)
48. S. Xuan, Y.-X.J. Wang, J.C. Yu, K.C.-F. Leung, Chem. Mater. **21**, 5079 (2009). https://doi.org/10.1021/cm901618m
49. E. Shah, H.P. Soni, RSC Adv. **3**, 17453 (2013). https://doi.org/10.1039/C3RA41285G
50. E. Shah, P. Mahapatra, A.V. Bedekar, H.P. Soni, RSC Adv. **5**, 26291 (2015). https://doi.org/10.1039/C5RA02249E
51. M. Kakihana, T. Nagumo, O. Makoto, H. Kakihana, J. Phys. Chem. **91**, 6128 (1987). https://doi.org/10.1021/j100308a015
52. T.K. Jain, M.A. Morales, S.K. Sahoo, D.L. Leslie-Pelecky, V. Labhasetwar, Mol. Pharm. **2**, 194 (2005). https://doi.org/10.1021/mp0500014
53. H.B. Na, I.C. Song, T. Hyeon, Adv. Mater. **21**, 2133 (2009). https://doi.org/10.1002/adma.200802366
54. B.O. Kjos, R.L. Ehman, M. Brant-Zawadzki, W.M. Kelly, D. Normal, T.H. Newton, AJNR. **6**, 144 (1985). https://doi.org/10.2214/ajr.144.6.1157
55. J. Wan, X. Jiang, H. Li, K. Chen, J. Mater. Chem. **22**, 13500 (2012). https://doi.org/10.1039/C2JM30684K
56. Y. Bao, J. Sherwood, Z. Sun, J. Mater. Chem. C. **6**, 1280 (2018). https://doi.org/10.1039/C7TC05854C
57. V.C. Pierre, M. Botta, S. Aime, K.N. Raymond, J. Am. Chem. Soc. **128**, 5344 (2006). https://doi.org/10.1021/ja057805x
58. E.J. Werner, A. Datta, C.J. Jocher, K.N. Raymond, Angew. Chem. Int. Ed. **47**, 8568 (2008). https://doi.org/10.1002/anie.200800212
59. N. Bloembergen, L.O. Morgan, J. Chem. Phys. **34**, 842 (1961). https://doi.org/10.1063/1.1731684
60. I. Solomon, N. Bloembergen, J. Chem. Phys. **25**, 261 (1956). https://doi.org/10.1063/1.1742867

Authors and Affiliations

Bindi Sanghavi[1] · Sucheta De Mondal[1] · Urja Verma[2] · Suresh Balakrishnan[2] · Sk Riyajuddin[3] · Kaushik Ghosh[3] · Mitesh Sarkar[4] · Hemant P. Soni[1]

✉ Sucheta De Mondal
suchetade16@gmail.com

✉ Hemant P. Soni
drhpsoni@yahoo.co.in; hemant.soni-chem@msubaroda.ac.in

[1] Department of Chemistry, Faculty of Science, The Maharaja Sayajirao University of Baroda, Vadodara, Gujarat 390 002, India

[2] Department of Zoology, Faculty of Science, The Maharaja Sayajirao University of Baroda, Vadodara, Gujarat 390 002, India

[3] Institute of Nano Science & Technology, Phase-10, Sector-64, Mohali, Punjab 160062, India

[4] Department of Physics, Faculty of Science, The Maharaja Sayajirao University of Baroda, Vadodara, Gujarat 390 002, India

Research on Chemical Intermediates
https://doi.org/10.1007/s11164-023-05017-3

Fe_3O_4@L-arginine and Fe_3O_4@L-histidine nanoparticles for one-pot solvent-free sequential Knoevenagel–Michael addition reactions

Bindi Sanghavi[1] · **Hemant P. Soni**[1]

Received: 3 January 2023 / Accepted: 14 April 2023

Abstract

Fe_3O_4@L-Arginine and Fe_3O_4@L-Histidine nanoparticles (NPs) are synthesized and explored as catalysts for the sequential Knoevenagel condensation and Michael addition reactions (KMS). The reaction parameters like the amount of catalyst, temperature, and solvent systems are optimized for both of the catalysts for the Knoevenagel condensation reaction. It was observed that the developed catalyst systems work well under solvent-free conditions at 80 °C. Excellent to high yield was achieved in the corresponding Knoevenagel adducts (up to 97%), in turn, delivered good yield in Michael products (up to 70%). Surprisingly, Fe_3O_4@L-Hist NPs did not show any catalytic activity for the sequential Michael addition. The probable reasons for the high activities of Fe_3O_4@L-Arg NPs for KMS have been discussed. The catalyst was also recovered and reused for 5 cycles with equal performance in terms of activity and selectivity. The optimized protocol for sequential Knoevenagel condensation and Michael addition reaction can result in high isolated yields with saving in the cost of solvent and falls under the domain of green chemistry.

Keywords Fe_3O_4 nanoparticles · Knoevenagel condensation · Michael addition reaction · Solvent-free condition · E-factor · Sequential reactions

Introduction

It is difficult to design heterogeneous catalytic one-pot multicomponent reactions (COP-MCRs). For these kinds of reactions to occur, the correct reactants and reagents must first be present at a single catalytic site, and then the bond-making and breaking processes must precisely take place in the available spatiotemporal regime, leading to the target product via a stable transition state. Any disturbance

---

✉ Hemant P. Soni
hemant.soni-chem@msubaroda.ac.in; drhpsoni@yahoo.co.in

[1] Department of Chemistry, Faculty of Science, The Maharaja Sayajirao University of Baroda, Vadodara, Gujarat 390 002, India

during this phase has the potential to alter the outcome of the reaction. The process can be sped up by using a solvent or additive that can stabilize the transition state through H-bonding or electrostatic interactions. The enzyme can accomplish this task effectively in nature. The amino acid residues at the catalytic site in the hydrophobic enzymatic grooves can effectively stabilize the transition state, resulting in the formation of the desired product with no by-products or waste [1]. To synthesize a variety of commercially significant products using green methods, it is necessary to mimic these natural enzymatic processes in the laboratory. To do this, protocols involving MCRs that take place in a single pot either sequentially (known as tandem reactions) or in a cascade (known as dominos reactions) fashion have been developed [2]. Compared to enzyme/homogeneous catalysis, MCRs employing heterogeneous catalysis in organic synthesis have advantages such as greater atom economy, atom usage, and selectivity can be obtained with time, cost, and energy savings [3–6]. Here, we investigated the tandem Knoevenagel–Michael addition events at a single catalytic site, which result in the products possessing a tri-substituted C–C bond in the molecular framework.

In a classic Knoevenagel reaction, the nucleophilic addition of a carbanion of an active methylene compound with an electron-withdrawing group to a carbonyl compound is followed by dehydration. This generates trisubstituted alkenes with an E-configuration. A basic mix of piperidine (pK_{aH} 11) and pyridine (pK_{aH} 5.5) is used as a catalyst [7–10]. Alternative catalytic systems were developed to carry out the neat and clean reaction with a smaller value of the E-factor as a consequence of the environmental concerns regarding the basic catalyst mixture. A variety of amino acids, such as -alanine [11], L-proline [12], L-histidine and L-arginine [13], guanidine [14], Lewis acids, such as $ZnCl_2$ [15], $TiCl_4$ [16], MgF_2 [17], and $CuCl_2$ [18], as well as surfactants, such as benzyl triethylammonium chloride [19], were investigated. Furthermore, heterogeneous catalysts such as organic–inorganic hybrid silica tagged with imidazolium and dihydro imidazolium salts [20], organic amines supported on inorganic solid-acid surfaces [21], silica-L-proline in the liquid phase [22], P4VP/Al_2O_3–SiO_2 [23], $HClO_4$–SiO_2 [24], Ni–SiO_2 [25], modified silica gel [26], magnetic hydroxyapatite-encapsulated γ-Fe_2O_3 nanoparticles [27], MCM-41 [28], MgO/ZrO_2 [29], zeolites [30–34], clays [35] were also employed as catalytic systems. These catalysts have good activity in terms of yield, but high temperature, prolonged reaction times, and catalyst recycling are still problems.

Therefore, the literature review mentioned above stresses the need for the generation of heterogeneous catalysts with the reaction sites basic in nature as well as additional environmental features like recovery and recycling. The best choice in this direction should be iron oxide-based nanoparticles (NPs) capped by amino acid functionalities. Studying the activity of the amino acid in constrained conformations while adsorbed on the magnetic surface might be intriguing. During enzymatic activities, amino acid molecules, and specifically the histidine residue of the enzymes, are known for their proton shuttling. The Knoevenagel reaction involves a similar proton shuttle mechanism [36]. Therefore, it would be preferable to retain the amino acid's molecular conformation and mimic enzyme-like activity under the reaction conditions. In light of this, we developed iron oxide nanoparticles with

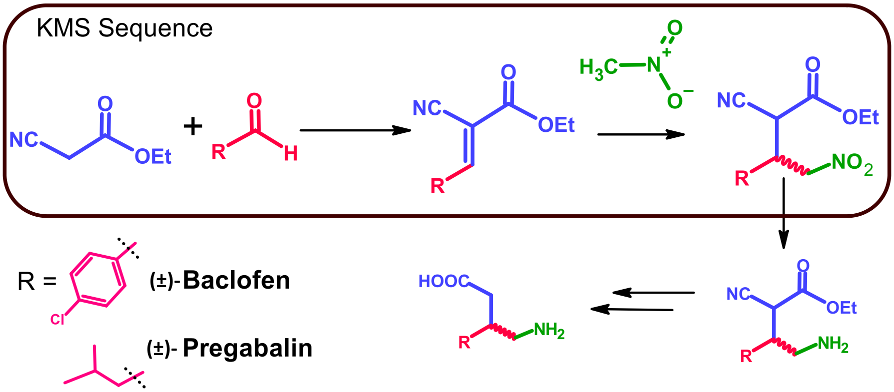

Scheme 1. Synthesis scheme involving KMS sequence leading towards pharmaceutically important drugs

L-histidine and L-arginine caps (Fe_3O_4@L-Hist and Fe_3O_4@L-Arg NPs, respectively) for the Knoevenagel reaction.

Now, from the standpoint of the pot economy, it would be advantageous to combine the sequential Michael addition of nitromethane, which is also catalyzed by the same developed base catalytic systems. For the synthesis of several key pharmaceutically important compounds, the Knoevenagel–Michael sequence (KMS) is necessary. The synthesis of (±)-Baclofen (4-amino-3-(4-chlorophenyl)butyric acid) and Pregabalin (Lyrica®) (3-isobutyl-γ-amino butyric acid) are two examples involving KMS. The conventional method for making the basic building blocks of these drugs involves Knoevenagel condensation, 1,4-addition of cyanide, hydrolysis of the resulting β-cyano diester, decarboxylation, reduction, and optical resolution of the resulting racemates (if necessary) (see Scheme 1) [37].

In the current study, we performed one-pot KMS of several aromatic aldehydes in the presence of as-synthesized catalysts under solvent-free conditions, producing precursors of the aforementioned drug molecules. We achieved high conversion and reaction yield in a short time. The catalysts were conveniently removed from the reaction mixture and successfully recycled for up to five cycles.

Experimental

Ethyl cyanoacetate, 4-nitro benzaldehyde, $FeCl_3·6H_2O$, L-histidine, L-arginine, ethyl acetate, and petroleum ether 60–80 were purchased from Loba Chemie Pvt. Ltd. Benzaldehyde, 4-chloro benzaldehyde and acetaldehyde were purchased from Spectrochem India. 4-Bromo benzaldehyde, 2- bromo benzaldehyde, 4-methyl benzaldehyde, and 4-methoxy benzaldehyde were purchased from TCI Chemicals (India) Pvt. Ltd. Propionaldehyde was purchased from S. D. Fine Chemical Ltd., India. $FeCl_2.4H_2O$ was purchased from Merck Life Science Private Limited. All the chemicals were used without further purification.

Synthesis of Fe_3O_4@AA NPs

For the preparation of L-arginine coated Fe_3O_4 NPs, $FeCl_3$ anhydrous (0.08 mmol) and $FeCl_2$ (0.04 mmol) were mixed in 50 mL deionized water in a round-bottom flask and the mixture was stirred at 70 °C for 15 min. Then, 10 mL aqueous solution of L-arginine (0.04 mmol) was drop-wise added and the reaction mixture was stirred for 20 min at the same temperature. Then, an aqueous solution of NH_4OH (10.0 mL) was instantly injected and the reaction mixture was stirred at 6000 rpm for 1 h. All the processes were carried out under a nitrogen atmosphere. After that, the resulting material was centrifuged, washed with deionized water and ethanol, and dried at 80 °C in an oven for 12 h. Fe_3O_4@L-histidine NPs were synthesized using the same procedure with L-histidine (0.04 mmol) dissolved in 10.0 mL water.

General procedure for the Knoevenagel condensation reaction

Aldehyde (1.0 mmol), ethyl cyanoacetate (1.0 mmol), and catalyst (80.0 mg) were mixed in the RBF and stirred vigorously at 80 °C in an oil bath. The progress of the reaction was monitored on the TLC plate. After the completion of the reaction, the catalyst was magnetically separated from the reaction mixture. The final isolated product was obtained followed by column chromatography using EtOAc: petroleum ether system.

General procedure for the Michael addition reaction

Nitromethane (2.0 mmol) and catalyst (80.0 mg) were added to the RBF and stirred vigorously at 80 °C. The progress of the reaction was monitored on the TLC plate. After completion of the reaction, the catalyst was magnetically separated from the reaction mixture. The final isolated product was obtained followed by column chromatography using EtOAc:petroleum ether solvent system.

General procedure for sequential Knoevenagel and Michael addition reaction

In a two necked RBF attached with air condenser and silica-gel guard tube, benzaldehyde (1.0 mmol), ethyl cyanoacetate (1.0 mmol), and Fe_3O_4@L-Arg NPs as catalyst (80.0 mg) were mixed, and stirred vigorously over the magnetic stirrer. The temperature of the reaction was slowly raised to 80 °C, and the reaction was allowed to continue for 2.5 h at this temperature. Then, nitromethane (2.0 mmol) was injected instantly in the reaction mixture with vigorous stirring. The reaction was continued for further 6 h by maintaining the temperature at 80 °C. Then, the catalyst was separated on applying the magnet outside the RBF, the mixture was decanted followed by column chromatography using EtOAc: petroleum ether solvent system.

General procedure for the recovery of catalyst for sequential Knoevenagel–Michael addition reaction

After completion of the reaction, the catalyst was separated with a magnet and the solvent was evaporated. The recovered catalyst was washed with ethanol and dried and reused under the same conditions as the first run at least 5 times and gave a corresponding product of KMS in high yield and selectivity.

(E)-Ethyl- 2-cyano-3-phenylacrylate (2a)

White solid crystals (m.p. 49–51 °C). FTIR (KBr, cm^{-1}). 2981 (–C–H, stretching, sp2), 2939(–C–H, stretching, sp^3), 2222 (–CN), 1726 (–C=O ester), 1606 (–C=C), 1444–15,720 (–C=C, Ar). ^{1}HNMR (400 MHz, $CDCl_3$) δ: 1.43 (CH_3, t, $J = 7.2$ Hz, 3H), 4.42 (CH_2, q, $J = 7.2$ Hz, 2H), 7.49–7.59 (ArH, m, $J = 7.2$ Hz, 3H), 7.99–8.01 (ArH, d, $J = 8.4$ Hz, 2H), 8.27 (–CH, s, 1H). ^{13}CNMR (400 MHz, $CDCl_3$) δ: 14.2 (–CH_3), 62.8(–O–CH_2), 102.9 (–C–CN), 115.5 (–CN), 129.3, 131.1, 131.5, 133.4, 155.1, 162.5 (–C=O). ESI–MS (m/z) = 201.2 [M + H] + (Fig. S4—S7).

(E)-Ethyl-2-cyano-3-(4-nitrophenyl) acrylate (2b)

Yellow solid crystals (m.p. 157–159 °C). FTIR (KBr, cm^{-1}). 3096 (–C–H, stretching, sp^2), 2993 (–C–H, stretching, sp^3), 2225 (–CN), 1720 (–C=O, ester), 1594, 1268 (–NO_2), 1415–1616 (–C=C, Ar), 1007 (–C=O, ester). ^{1}HNMR (400 MHz, $CDCl_3$) δ: 1.4 (–CH_3, t, $J = 7.2$ Hz, 3H), 4.4 (CH_2, q, $J = 7.2$ Hz, 2H), 8.1 (ArH, d, $J = 8.8$ Hz, 2H), 8.32–8.36 (Ar H, d, $J = 8.8$ Hz, 2H), 8.38 (–CH, s, 1H). ^{13}CNMR (400 MHz, $CDCl_3$) δ: 14.1 (–CH_3), 63.4 (–O–CH_2), 107.3 (–C–CN), 114.6 (–CN), 124.4, 131.5, 136.9, 149.7 (–C–NO_2), 151.8 (–C=C), 161.4 (–C=O). ESI–MS (m/z) = 246.08 $[M + H]^+$ (Fig. S8 –S11).

(E)-Ethyl 2-cyano-3-(4-methoxyphenyl) acrylate (2c)

White solid crystals (m.p. 109–111 °C). FTIR (KBr, cm^{-1}). 1435, 1513, 1561 (–C=C, Ar), 1717 (–C=O), 2215 (–CN), 2843, 2992 (–CH, str), 3025 (–CH, str). ^{1}HNMR (400 MHz, $CDCl_3$) δ: 1.42 (–CH_3, t, $J = 7.2$ Hz, 3H), 3.90 (–O–CH_3, s, 3H), 4.40 (–CH_2, q, $J = 7.0$ Hz, 2H), 6.99–7.01 (Ar H, d, $J = 8.8$ Hz, 2H), 8.0 (ArH, d, $J = 8.8$ Hz, 2H), 8.2 (=CH, s, 1H). ^{13}CNMR (400 MHz, $CDCl_3$) δ: 14.2 (–CH_3), 55.6(–OCH_3), 62.5 (–OCH_2), 99.3 (–C–CN), 116.3 (–CN), 114.8, 124.3, 133.7, 154.5, 163.2, 163.8 (–C=O). ESI–MS (m/z) = 231.28 $[M + H]^+$ (Fig. S12 –S15).

(E)-Ethyl-2-cyano-3-(p-tolyl) acrylate (2d)

White solid crystals (m.p. 110–113 °C). FTIR (KBr, cm^{-1}). 3029 (–C–H, *stretching*, sp^2), 2993 (–C–H, stretching, sp^3), 2216 (–CN), 1724 (–C=O, ester), 1420–1596 (–C=C–Ar), 1093 (–C–O, ester). ^{1}HNMR (400 MHz, $CDCl_3$) δ: 1.42 (CH_3, t, $J =$ 7.2 Hz, 3H), 2.44 (CH_3, s, 3H), 4.41 (CH_2, q, $J = 6.8$ Hz, 2H), 7.6 (ArH, d, $J =$

8.8 Hz, 2H), 7.8 (Ar H, d, J = 8.4 Hz, 2H), 8.2 (=CH, s, 1H). ^{13}CNMR (400 MHz, $CDCl_3$) δ: 14.2 (–CH_3), 21.9 (Ar– CH_3), 62.6 (O–CH_2), 101.5 (–C–CN), 115.8 (–CN), 128.8, 130.0, 131.2, 144.7, 162.8 (–C=O), 155.0 (–C=C). ESI–MS (m/z) = 215.19 $[M + H]^+$ (Fig. S16 –S19).

(E)-Ethyl-2-cyano-3-(4-chlorophenyl) acrylate (2e)

White solid crystals (m.p. 159–160 °C). FTIR (KBr, cm^{-1}). 3431 (–C–H, stretching, sp^2), 2954 (–C–H, stretching, sp^3), 2223 (–CN), 1726 (–C=O, ester), 1411–1611 (–C=C, Ar), 1206 (–C–O, ester), 1081 (Ar–Cl). ^{1}HNMR (400 MHz, $CDCl_3$) δ: 1.43 (–CH_3, t, J = 7.2 Hz, 3H), 4.43 (–CH_2, q, J = 7.2 Hz, 2H), 7.48 (Ar H, d, J = 6.8 Hz, 2H) 7.93–7.96 (Ar H, d, J = 6.8 Hz, 2H), 8.22 (= CH, s, 1H). ^{13}CNMR (400 MHz, $CDCl_3$) δ: 14.2 (–CH_3), 62.9 (–O–CH_2), 103.4 (–C–CN), 115.3 (–CN), 129.7, 132.2, 139.6, 153.5, 162.3 (–C=O). ESI–MS (m/z) = 235.09 $[M + H]^+$(Fig. S20 –S23).

(E)-Ethyl-2-cyano-3-(4-bromophenyl) acrylate (2f)

White solid crystals (m.p. 80 –82 °C). FTIR (KBr, cm^{-1}) 3430 (–C–H, stretching, sp^2) 2952 (–C–H, stretching, sp^3), 2222 (–CN), 1725 (–C=O, ester), 1487–1611 (Ar, C=C), 1205 (–C–O, ester), 1094 (Ar–Br). ^{1}HNMR (400 MHz, $CDCl_3$) δ: 1.4 (CH_3, t, J = 7.2 Hz, 3H), 4.4 (CH_2, q, J = 6.8 Hz, 2H), 7.6 (Ar H, d, J = 8.8 Hz, 2H), 7.8 (ArH, d, J = 8.4 Hz, 2H), 8.2 (=CH, s, 1H). ^{13}CNMR (400 MHz, $CDCl_3$) δ:14.2 (–CH_3), 62.9 (–O–CH_2), 103.6 (–C–CN), 115.3 (–CN), 128.3, 130.2, 132.2, 132.7, 153.6 (–C=C), 162.2 (–C=O). ESI–MS (m/z) = 280.06 $[M + H]^+$ (Fig. S24 –S27).

(E)-Ethyl-2-cyano-3-(2-bromophenyl) acrylate (2 g)

White solid crystals (m.p. 81–83 °C). FTIR (KBr, cm^{-1}) 3430 (–C–H, stretching, sp^2) 2952 (–C– H, stretching, sp^3), 2222 (–CN), 1725 (–C=O, ester), 1487–1611 (Ar, C=C), 1205 (–C–O, ester), 1094 (Ar–Br). ^{1}HNMR (400 MHz, $CDCl_3$) δ: 1.4 (CH_3, t, J = 7.2 Hz, 3H), 4.4 (CH_2, q, J = 6.4 Hz, 2H), 7.2 (Ar H, t, J = 7.6 Hz, 1H), 7.3 (Ar H, t, J = 7.6 Hz, 1H), 7.5 (Ar H, d, J = 8.0 Hz, 1H), 8.0 (ArH, d, J = 7.6 Hz, 1H), 8.6 (=CH, s, 1H). ^{13}CNMR (400 MHz, $CDCl_3$) δ: 14.2 (–CH_3), 63.0 (O–CH_2), 106.4 (C–CN), 114.7 (–CN), 126.6, 128.1, 130.1, 131.7, 133.6, 133.7, 153.9 (–C=C), 161.8 (–C=O). ESI–MS (m/z) = 280.06 $[M + H]^+$ (Fig. S28 –S31).

Ethyl-2-cyano-4-nitro-3-phenyl butanoate (3a)

Colorless oil. ^{1}HNMR (400 MHz, $CDCl_3$). δ: 7.41 (m, J = 7.6 Hz, 10 H), 5.05 (m, J = 6.8 Hz, 4H), 4.27 (m, J = 7.6 Hz, 6H), 3.95 (m, J = 5.6 Hz, 2H), 1.17 (t, J = 7.2 Hz, 6H). ^{13}CNMR (400 MHz, $CDCl_3$) δ: 13.8 (–CH_3), 41.5 (–C–CH_2), 43.1 (–C–CN), 63.7 (–OCH_2–), 76.3 (–CH_2–NO_2), 114.4 (–CN), 127.5, 129.3, 129.5, 134.5 (–C=C), 163.9 (–C=O) (Fig. S32 –S33).

Ethyl 2-cyano-4-nitro-3-(4-nitrophenyl) butanoate (3b)

Colorless oil.^{1}HNMR (400 MHz, $CDCl_3$) δ: 8.27 (m, J = 6.8 Hz, 4H), 7.5 (m, J = 8.0 Hz, 4H), 5.06 (m, J = 7.6 Hz, 4H), 4.43 (m, J = 5.6 Hz, 6H), 4.02 (m, J = 6.8 Hz, 2H), 1.28 (t, J = 7.2 Hz, 3H) (Fig. S34).

Ethyl 2-cyano-4-nitro-3-(4-methoxy phenyl) butanoate (3c)

Colorless oil. ^{1}HNMR (400 MHz, $CDCl_3$) δ: 7.26 (m, J = 7.0 Hz, 4H), 6.90 (m, J = 8.8 Hz, 4H), 5.03 (m, J = 6.6 Hz, 4H), 4.26 (m, J = 6.8 Hz, 6H), 3.91 (m, J = 5.6 Hz, 2H), 3.81 (s, 6H), 1.27 (t, J = 4.8 Hz, 3H) (Fig. S35).

Ethyl 2-cyano-4-nitro-3(4-methylphenyl) butanoate (3d)

Colorless oil. ^{1}HNMR (400 MHz, $CDCl_3$) δ: 7.18 (m, J = 6.8 Hz, 8H), 5.04 (m, J = 6.4 Hz, 4H), 4.7 (m, J = 7.2 Hz, 6H), 4.27 (m, J = 6.8 Hz, 2H), 2.35 (s, 3H), 1.16 (t, J = 7.2 Hz, 6H) (Fig. S36).

Characterization

X-ray powder diffraction (XRD) pattern was obtained using X-ray powder diffractometer (Philips X'pert MPD system) with Cu Kα radiation, λ = 0.15418 nm. The BET-specific surface area (SBET) was determined by nitrogen adsorption (Micrometrics ASAP 2020, USA) via a multipoint BET method using the adsorption data in the relative pressure (P/P^o) range of 0.0–1.0. The samples were degassed at 80 ^{o}C before Brunauer–Emmett–Teller (BET) measurements. Desorption isotherm was used to determine the pore-size distribution using the Barret– Joyner–Halendar (BJH) method, assuming a cylindrical pore model. The nitrogen adsorption volume at the relative pressure (P/P^o) range of 0.997 was used to determine the pore volume and average pore size. The morphology of the samples was examined by FESEM (JEOL-JSM-7100F). Particle size with elemental mapping was carried out by TEM (JEOL-JEM-2100) at 200 kV. FT-IR spectra of all compounds were recorded with Bruker FTIR spectrometer using KBr pellets in the range of 400 to 4000 cm^{-1}. UV– visible absorption spectra were recorded on a Perkin Elmer Lambda 35 and PL spectra were recorded on a Jasco FP-6300 spectrophotometer using a Xenon lamp as an excitation source at 280 nm. All measurements were made at 25 °C in methanol. HRMS was recorded on Xevo G2-S Q Tof (Waters, USA), and TG analysis was recorded on Exstar TG/DTA7000 from 30 to 550 °C with a heating rate of 10 °C. The sample size was between 7–8 mg. The ^{1}H NMR and ^{13}C NMR were recorded on Bruker Avance 400 MHz spectrometers using TMS as an internal standard in $CDCl_3$.

Results and discussion

Powder XRD was used to investigate the phase of as-synthesized Fe_3O_4@L-Arg and Fe_3O_4@L-Hist nanoparticles. The magnetite phase is revealed by the diffraction pattern shown in Fig. 1. The magnetite phase of Fe_3O_4 NPs with inverted spinel structure is confirmed by the X-ray diffraction peaks at 2θ values of 31.0, 36.4, 43.8, 53.5, 57.7, and 63.0°, which, for both systems, correspond to the (220), (311), (400), (422), (511) and (440) planes, respectively (JCPDS No. 82–1533) (Fig. 1). The particle size was determined by the Debye–Scherrer formula ($L = 0.9\lambda/\beta \cos\theta$) and the FWHM (Full Width at Half Maximum) value [38] of the major peak for (311) planes in the range of 20.45 and 16.76 nm, respectively. It can be observed that adsorption of amino acids does not affect the XRD pattern.

Transmission Electron Microscopy (TEM) was used to directly observe the morphology of the sample (Fig. 2). Figure 2 shows that both catalytic systems—Fe_3O_4@

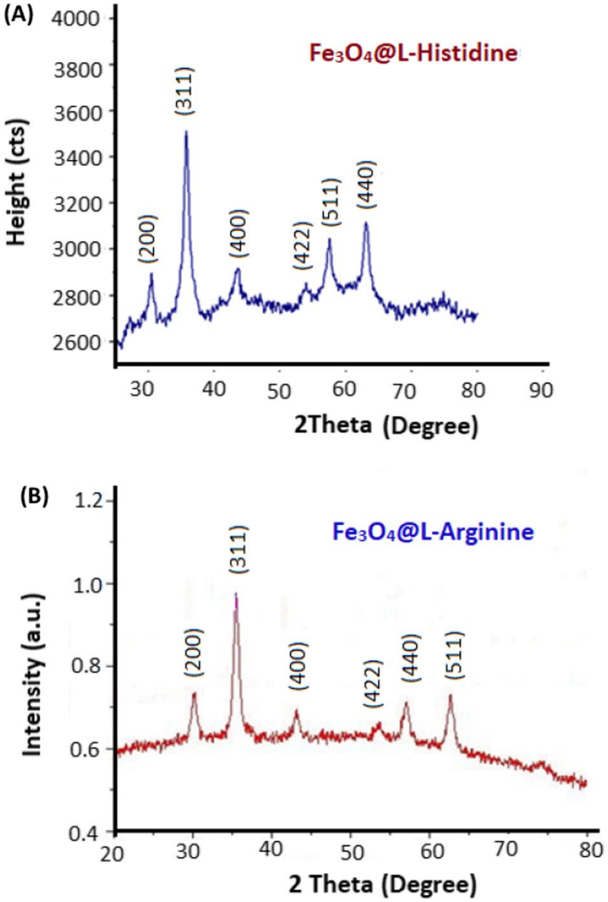

Fig. 1 Powder X-ray diffraction patterns of as-synthesized **a** Fe_3O_4@L-Hist and **b** Fe_3O_4@L-Arg NPs

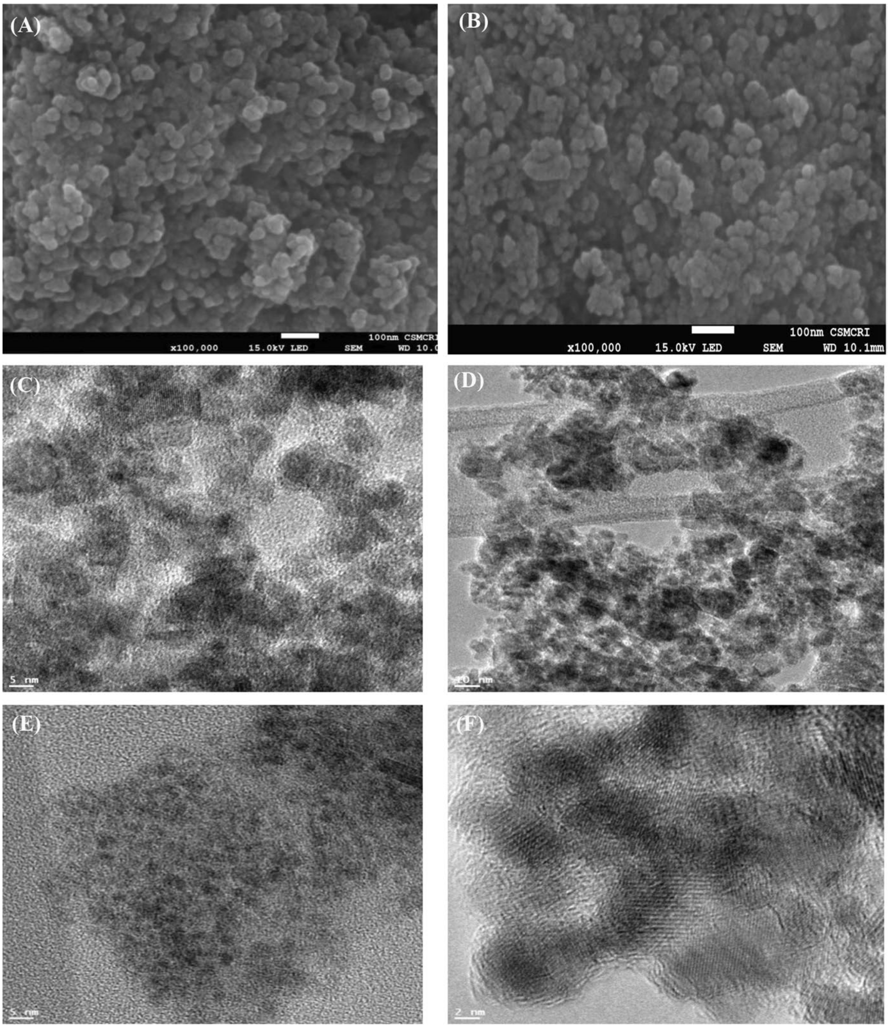

Fig. 2 HRSEM images of **a** Fe_3O_4@L-Arg **b** Fe_3O_4@L-Hist NPs. HRTEM images and lattice fringes at higher magnification of as-synthesized **c**, **d** Fe_3O_4@L-Arg and **e**, **f** Fe_3O_4@L-Hist NPs

AA (Amino Acids) NPs—display spherical morphology in the size range of 2–10 nm. Spherical particles with a crystallite size of 5–10 nm are visible in the HRTEM images. The lattice fringes of the (400) exposed planes are separated by 0.18 nm. The HRSEM images also support these observations.

FTIR spectroscopy is one of the best techniques for investigating the interactions of ligand molecules with the host surface [39–43]. The FTIR spectra of pristine Fe_3O_4, free L-arginine and L-histidine, Fe_3O_4@L-Hist, and Fe_3O_4@L-Arg NPs are presented in Figure S2. For pristine Fe_3O_4 NPs, the absorption between 600 and 650 cm^{-1} is due to the Fe–O stretching of the inverse spinel system. The carboxylate ion of the amino acid ligand can coordinate with surface Fe ions in either a monodentate or a bidentate (chelating) mode [44, 45]. These can be proven by the COO^- stretching vibration frequencies. Two primary modes of vibration for free carboxylate ions in acetate form are $\nu_{as(COO^-)}$ and symmetric $\nu_{s(COO^-)}$ stretching at 1583 and 1422 cm^{-1}, respectively. For Fe_3O_4@L-Arg NPs, the $\nu_{as(COO^-)}$ of carboxylate ions is at 1562 cm^{-1} and $\nu_{s(COO^-)}$ is at 1472 cm^{-1}. In coordination with surface Fe ions, $\nu_{as(COO^-)}$ decreases while $\nu_{s(COO^-)}$ increases, indicating that the carboxylate ion of amino acid is coordinated bidentately. Additionally, Δ ($\nu_{as(COO^-)}$—$\nu_{s(COO^-)}$) is greater than Δ' ($\nu'_{as(COO^-)} - \nu'_{s(COO^-)}$), where Δ is the difference between the absorption bands for free carboxylate ions and Δ' for metal-bound carboxylate ions, indicating bidentate coordination [43]. While the $\nu_{as(COO^-)}$ of carboxylate ions shows at 1588 and $\nu_{s(COO^-)}$ at 1413 cm^{-1} in the case of Fe_3O_4@L-Hist NPs, suggesting a similar type of bidentate coordination. From the UV–vis spectra, it can be inferred that L-histidine absorbs at 290 nm due to $n \rightarrow \pi^*$ transition and it fluoresces at 450 nm when excited at the same absorption wavelength which remains unaltered after adsorption on the surface of Fe_3O_4 NPs (Fig. S3). Based on these investigations, we suggest the bidentate type of amino acid molecule orientations on the surface of magnetic NPs (Fig. 3).

A thermogravimetry analysis of the freshly synthesized NPs was conducted in order to further validate the presence of amino acid molecules adsorbed on the surface. Figure 4 shows the thermograms of pristine iron oxide (Fe_3O_4), Fe_3O_4@L-Hist, and Fe_3O_4@L-Arg NPs, which can be utilized for quantification of the material's degradation behaviour. In the TG analysis temperature range, iron oxide doesn't lose weight. On the other hand, both of the Fe_3O_4@AA samples exhibit two-stage degradation. Due to the degradation of surface-adsorbed organic material, Fe_3O_4@L-Arg and Fe_3O_4@L-Hist NPs displayed severe weight loss above 150 °C and 150–200 °C, respectively, and persisted up to 400 °C for both samples. The weight loss at around 100 °C is due to the surface-adsorbed water molecules. These studies demonstrate that amino acid molecules are present on the surface of Fe_3O_4 nanoparticles. On the

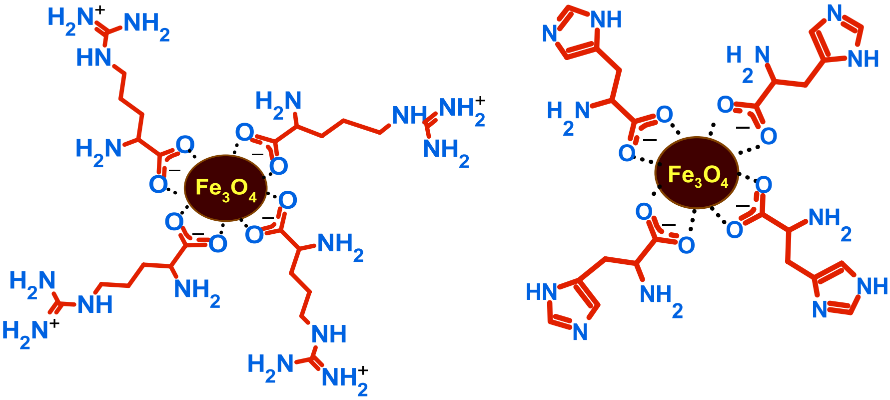

Fig. 3 Proposed interaction of L-arginine and L-histidine molecules with the surface of Fe_3O_4 NPs based on FTIR spectroscopy

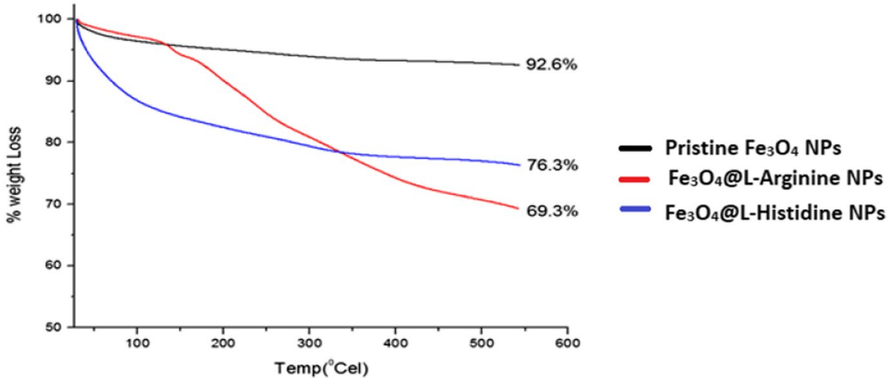

Fig. 4 Thermograms of pristineFe_3O_4, Fe_3O_4@L-Arg, and Fe_3O_4@L-Hist NPs. The % weight of the residues is shown at the end of the curves

basis of water loss and the %weight of residues left after heat treatment, the loading of L-arginine and L-histidine on the surface of NPs was calculated to be 23.3 and 16.3 per cent, respectively.

The nitrogen adsorption–desorption isotherms for the synthesized Fe_3O_4@L-Arg and Fe_3O_4@L-Hist NPs, as well as their computed BET surface area and pore volume, are shown in Fig. 5 and Table S1. The isotherms of Fe_3O_4@L-Arg and Fe_3O_4@L-Hist NPs are of type IV (BDDT classification), as seen in Fig. 5, with the H4 and H3 type of curves, respectively where the two branches are nearly horizontal and parallel throughout a large range of relative pressures (P/Po), suggesting the well-ordered mesoporous structure. In this situation, the amount of gas adsorbed increases as P/Po rises. Narrow pores that resemble slits are frequently linked to the type H4 curve [26, 46]. Fe_3O_4@L-Arg NPs have a much higher surface area than Fe_3O_4@L-Hist NPs, as can be seen in Table 1. The BET surface area and pore size studies show that both kinds of synthesized NPs systems are good for catalytic activities.

Fe_3O_4@L-Arg and Fe_3O_4@L-Hist NPs magnetization curves were plotted using a magnetic field gradient from −15,000 to + 15,000 Oe (Fig. 6). As can beseen in Fig. 6, Fe_3O_4@L-Arg NPs exhibit superparamagnetic behaviour with a Ms value of 61.5 emu/g while Fe_3O_4@L-Hist NPs exhibit paramagnetic behaviour with a very low Ms value of 0.25 emu/g [47, 48]. This investigation reveals the material's ability to become magnetized under the influence of a magnetic field and being recovered on removal of the field.

Optimization of reaction parameters for model Knoevenagel condensation reaction

The model Knoevenagel reaction was carried out under various sets of conditions involving different catalysts, Fe_3O_4@L-Arg or Fe_3O_4@L-Hist, their amounts, solvents, and temperature to optimize the reaction parameters.

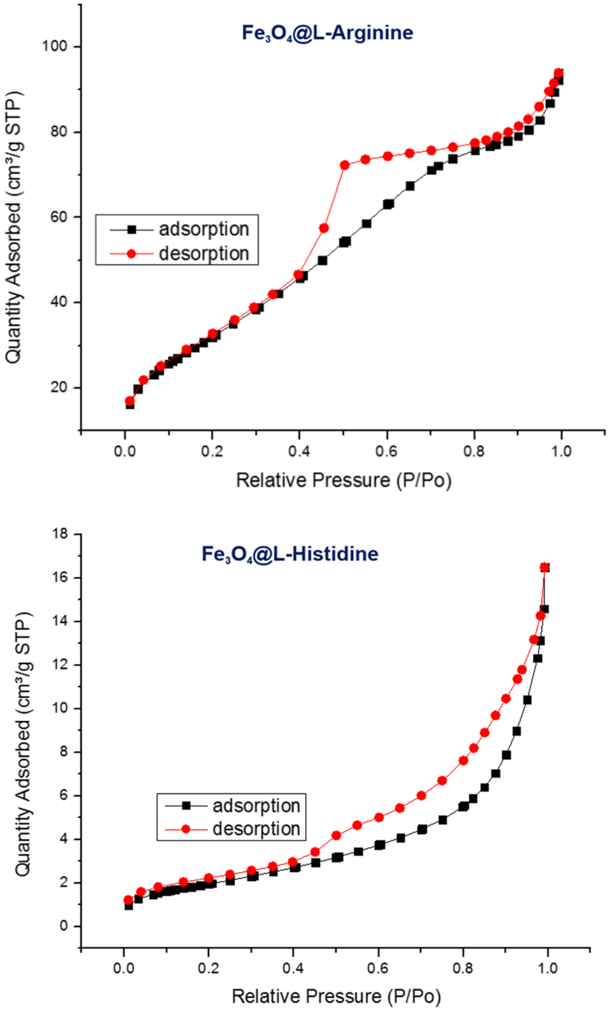

Fig. 5 Nitrogen adsorption–desorption isotherms of as-synthesized Fe_3O_4@L-Arg and Fe_3O_4@L-Hist NPs

In a model reaction, the Knoevenagel condensation of benzaldehyde (**1a**) and ethyl cyanoacetate was carried out by using the two as-synthesized catalytic systems. Table 1 shows that the reaction could not continued in the absence of the catalyst. Additionally, we conducted controlled reactions using free L-arginine and L-histidine as well as pristine Fe_3O_4 NPs. Due to the Lewis acidicproperties of Fe_3O_4 NPs, the reaction continued in the forward direction with a less yield of the product after 8 h at 80 °C. Due to the solvent-free condition, which is discussed later, the same result was observed when the reaction was conducted in the presence of free amino acids.

Table 1 Effect of different catalysts on Knoevenagel condensation reaction

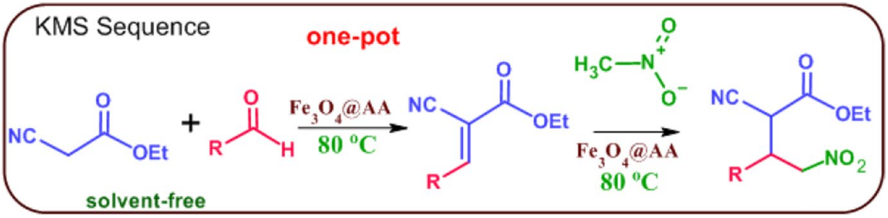

Sr. No.	Catalyst[a]	Yield[a,b] (%)
1	No Catalyst	–
2	Fe_3O_4	17
3	L-Arginine	32[c]
4	L-Histidine	29[c]
5	Fe_3O_4@L-Arg	94
6	Fe_3O_4@L-Hist	91

[a] Reaction conditions: Catalyst (80.0 mg), benzaldehyde (1.00 mmol), ethyl cyanoacetate (1.00 mmol), reaction temperature (80 °C), reaction time, 180 min

[b] Isolated yield

[c] Solvent-less condition

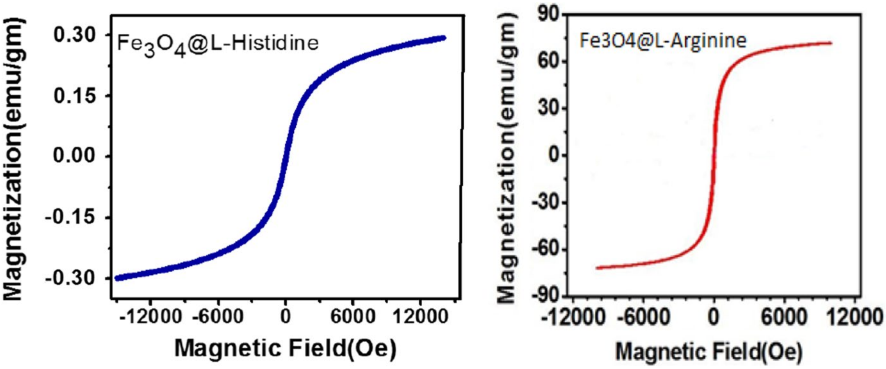

Fig. 6 M -H curves for as-synthesized **a** Fe_3O_4@L-Hist and **b** Fe_3O_4@L-Arg NPs

The amount of the catalyst had a significant impact on the reaction. The yield increased dramatically as the catalyst loading was increased, reaching up to 94% in the case of Fe_3O_4@L-Arg on 80 mg of loading (Table 2).

We tried out a range of temperatures for the model Knoevenagel condensation reaction carried out up to 180 min under the optimized conditions (Table 3). From 10 to 60 °C, the reaction rate was found to be quite slow and then increased

Table 2 Optimization of the amount of catalyst (Fe_3O_4@L-Arg and Fe_3O_4@L-Hist) for the model Knoevenagel condensation reaction[a,c]

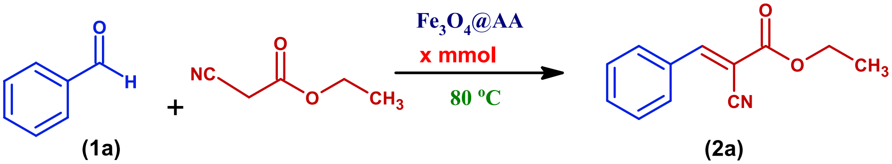

Sr. No.	Catalyst amount (mg)	Yield[b] (%)	
		Fe_3O_4@L-Hist	Fe_3O_4@L-Arg
1	5.0	43	46
2	10.0	57	59
3	20.0	61	66
4	30.0	74	80
5	50.0	85	89
6	80.0	85	94
7	100.0	85	94

[a] Reaction conditions: Benzaldehyde (1.00 mmol), ethyl cyanoacetate (1.00 mmol), reaction time: for Fe_3O_4@L-Hist-180 min and Fe_3O_4@L-Arg – 150 min, reaction temperature, 80 °C

[b] Isolated yield

[c] Solvent-less condition

Table 3 Optimization of temperature for Fe_3O_4@L-Arg and Fe_3O_4@L-Hist NPs mediated model Knoevenagel condensation reaction[a,c]

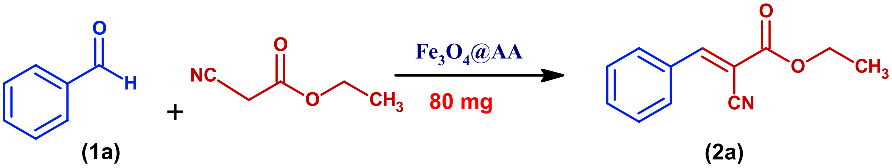

Sr. No.	Temperature (°C)	Yield[b,c] (%)	
		Fe_3O_4@L-Hist	Fe_3O_4@L-Arg
1	10	Trace	Trace
2	RT	39	44
3	40	46	53
4	60	82	91
5	80	85	94

[a] Reaction conditions: Catalyst (80.0 mg), benzaldehyde (1.00 mmol), ethyl cyanoacetate (1.00 mmol), reaction time: for Fe_3O_4@L-Hist-180 min and Fe_3O_4@L-Arg – 150 min

[b] Isolated yield

[c] Solvent-less condition

Table 4 Optimization of reaction time for Fe_3O_4@L-Arg and Fe_3O_4@L-Hist NPs mediated Knoevenagel condensation reaction[a,c]

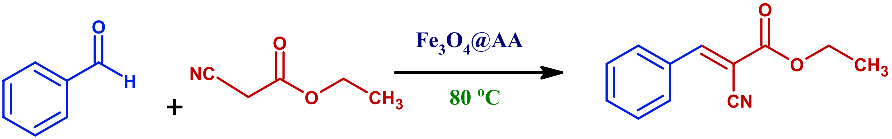

(1a) (2a)

Sr. No.	Time (mins)	Yield[b,c] (%)	
		Fe_3O_4@L-Hist	Fe_3O_4@L- Arg
1	30	20	37
2	60	35	58
3	120	63	79
4	150	71	94
5	180	82	94

[a] Reaction conditions: Catalyst (80.0 mg), benzaldehyde (1.00 mmol), ethyl cyanoacetate (1.00 mmol), reaction temperature, 80 °C

[b] Isolated yield

[c] Solvent-less condition

Table 5 Optimization of a solvent system for Fe_3O_4@L-Arg and Fe_3O_4@L-Hist NPs mediated Knoevenagel condensation reaction[a]

Sr. No.	Solvent	Temperature (°C)	Yield[b](%)	
			Fe_3O_4@L-Hist	Fe_3O_4@L-Arg
1	Solvent-free	80	91	94
2	Water	80	68	68
3	Ethanol	60	43	43
4	DCM	40	–	–
5	$CHCl_3$	50	10	10

[a] Reaction conditions: Catalyst (80.0 mg), benzaldehyde (1.00 mmol), ethyl cyanoacetate (1.00 mmol), time, for Fe_3O_4@L-Arg-150 min, and Fe_3O_4@L-Hist- 180 min, 80 °C

[b] Isolated yield

with an increase in temperature. At 80 °C, the reaction proceeded with the highest yield.

Time has a substantial impact on the reaction under evaluation. According to Table 4, for the Fe_3O_4@L-Arg and Fe_3O_4@L-Hist NPs mediated catalysis, the %yield increased and reached a maximum of 94 and 82% within 150 and 180 min, respectively.

For the model Knoevenagel condensation, both of the synthesized catalysts were utilized to evaluate different solvents and solvent-free conditions in order to maximize yield. Table 5 provides an overview of the outcomes. These findings support the notion that for both catalytic systems, solvent-free conditions yield the best outcomes.

To comprehend the electronic effects of substituent groups on the reaction, various aromatic and aliphatic aldehydes substituted with electron-donating and withdrawing groups were assessed (Table 6). It was observed that in the case of substituted aromatic aldehydes **1a–g** those with electron-withdrawing groups undergo a faster reaction than with electron-donating groups. In the case of aliphatic aldehydes **1 h-1i**, Knoevenagel condensation did not happen with ethyl cyanoacetate in the presence of catalysts Fe_3O_4@L-Hist and Fe_3O_4@L-Arg under the optimized conditions.

Furthermore, at optimal reaction conditions, Michael addition of the Knoevenagel product **2a-d** containing electron-donating and -withdrawing groups was performed using nitromethane. In contrast to electron-donating groups in the presence of Fe_3O_4@L-Arg at 80 °C, the Knoevenagel condensation adduct with electron-withdrawing groups produced a good yield of the Michael product **3a-d**. The sequential Michael reaction could not be catalysed by Fe_3O_4@L-Hist under the optimal reaction conditions (Table 7).

Recovery and recycling of Fe_3O_4@L-arginine and Fe_3O_4@L-histidine NPs

Additionally, the model sequential reaction's catalyst recovery was examined under optimal reaction conditions (Fig. S3). After the KMS reaction was finished, the reaction mixture was filtered and the catalyst was completely washed with ethanol, dried under vacuum at 70 °C, and reused for the succeeding reaction cycle. Under the present conditions, Fe_3O_4@L-Hist (for the Knoevenagel reaction) or Fe_3O_4@L-Arg (for the KMS reaction) can be recovered and reused at least five times. It is significant to notice that after 5 cycles, the catalytic activity is reduced.

Scheme 2 shows the proposed reaction mechanism based on the review of the literature and the results of the experiments. Consequently, the carboxylate group of the amino acid molecule interacts with the Fe_3O_4 surface Fe^{2+}/Fe^{3+} ions in a bidentate manner, leaving the amine group free (based on FTIR spectroscopy data). The surface-retained amine group produces imine (**I**) by nucleophilic addition to benzaldehyde. Now, the imine nitrogen atom is sufficiently basic to remove the acidic proton from the ethyl cyanoacetate active methylene group, which in turn initiates the nucleophilic attack of the resultant carbanion to produce the intermediate **II**. Lastly, the base-catalyzed mechanism makes the Knoevenagel product, which is a trisubstituted alkene **III**. Product **III** participates in the sequential Michael reaction as a Michael acceptor, followed by the addition of nitromethane, a Michael donor, which is initiated on the same catalytic site on the magnetic surface (Fe_3O_4@L-Arg) to give the final KMS product (Scheme 2).

Origin of reactivity

In the instance of the Knoevenagel reaction, it can be shown that the Fe_3O_4@L-Arg NPs exhibit stronger catalytic activity than the Fe_3O_4@L-Hist NPs, while the

Table 6 Knoevenagel condensation reaction between aromatic/aliphatic aldehydes and ethyl cyanoacetate catalyzed by Fe_3O_4@L-Arg and Fe_3O_4@L-Hist NPs[a].

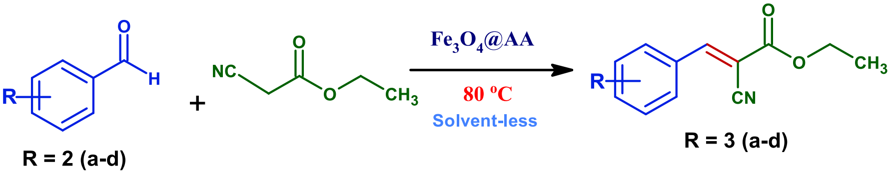

Aldehyde	Product	Time (mins)		Yield[b,c] (%)	
		Fe_3O_4@L-Hist	Fe_3O_4@L-Arg	Fe_3O_4@L-Hist	Fe_3O_4@L-Arg
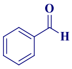 (1a)	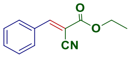 (2a)	180	150	91	94
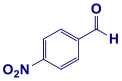 (1b)	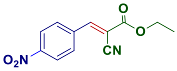 (2b)	75	50	94	97
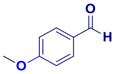 (1c)	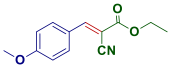 (2c)	180	150	89	90
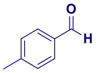 (1d)	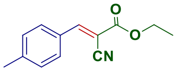 (2d)	180	150	87	89
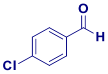 (1e)	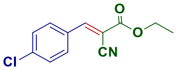 (2e) (2e)	90	75	92	95
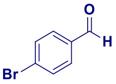 (1f)	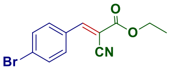 (2f)	90	70	91	93
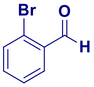 (1g)	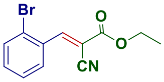 (2g)	90	73	90	91
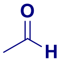 (1h)	–	180	150	–	–
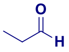 (1i)	–	180	150	–	–

[a] Reaction conditions: Catalyst (80.0 mg), aldehyde (1.00 mmol), ethyl cyanoacetate (1.00 mmol), reaction temperature, 80 °C

[b] Isolated yield

[c] Solvent-less condition

Fe_3O_4@L-Hist NPs catalytic system is completely inactive for the sequential Michael addition process. There could be two major reasons for this. (1) The effective delocalization of the positive charge on the side chain guanidine nitrogen makes L-Arginine more basic than L-histidine. In contrast to the amine group found in the imidazole ring of L-histidine, which has a pKaH of 6.5 (near neutrality), the guanidine amino group of L-arginine has a pKaH of 12. So, during the synthesis of NPs, both of the amino acid molecules get adsorbed and coordinated with surface Fe^{2+}/Fe^{3+} ions by the negatively charged carboxylate group. This happens because the reaction medium is basic due to the ammonia. Now, when these NPs systems are utilised as catalysts under solvent-free conditions, the 1^o amino group of L-arginine close to the surface carboxylate ion will be more basic due to the availability of a loan pair of electrons, as the side chain guanidine nitrogen atoms hold the proton more tightly. So, the 1° amine group of L-arginine acts as a basic catalytic site for the reaction under consideration. Instead, the side chain imidazole ring of L-histidine can’t hold the basic proton more tightly than that of L-arginine, and the 1° amine of the amino acid near the surface carboxylate ion becomes positively charged at a pH close to neutral [49]. Due to this, L-histidine becomes less basic and is less effective at base catalysis. Hence, it can catalyze the Knoevenagel reaction through the side chain imidazole –NH group but is not basic enough to carry out the sequential Michael addition reaction of nitromethane (Fig. 7) (2) the flexibility of the adsorbate amino acid molecular framework on the Fe_3O_4 nanoparticle surface. Due to the central three-carbon long "spacer," L-arginine can adopt a better molecular conformation and interact with the substrate aldehyde more easily to form imines, whereas L-histidine could not show reactivity under the optimal conditions because of the rigidity of the molecular framework on adsorption on the magnetic surface (Fig. 7).

Rahmati et al. reported free L-arginine and L-histidine as a catalyst for the Knoevenagel reaction [13]. They condensed various aromatic substituted aldehydes with malononitrile, ethyl cyanoacetate, or ethyl acetoacetate. When the reaction was run in aqueous media for 5–12 h at room temperature, they got good yields. Hence, the "free amino acid" can produce good results when the reaction is conducted "in water," but solvent-free conditions are favored when they are adsorbed on a suitable surface.

Table 8 lists the various catalytic systems designed for the Knoevenagel reaction along with their optimized reaction parameters and compares them to the developed NPs systems described in this study. It can be shown that malononitrile is a preferred substrate (because the methylene group may be easily activated by two nearby cyano groups) and that a fair yield can be obtained when it is condensed with aldehydes (Table 8). However, there are few reports of ethyl cyanoacetate condensing with aldehydes and the protocols that do achieve a moderate to low yield (Table 8). According to Table 8, the as-synthesized NPs catalytic system is a productive "green" catalyst for the Knoevenagel condensation reaction when no solvent is present. We also used the conventional formula from the literature to compute the E-factor, which we found to be 0.42 for the Fe_3O_4@L-Arg and 0.47 for the Fe_3O_4@L-Hist NPs catalyst systems, respectively (SI computation S1) [50]. These outcomes render the developed protocol truly "green."

Table 7 Fe_3O_4@L-Arg catalyzed sequential Michael addition reaction with Knoevenagel condensation product.[a]

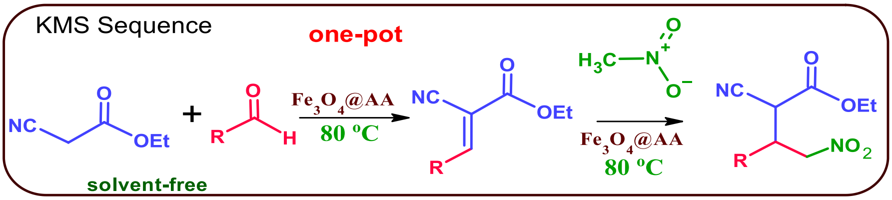

Knoevenagel adduct	Product	Time (h)	Yield[b] (%)	
			Fe_3O_4@L-Hist	Fe_3O_4@L-Arg
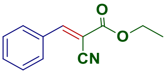 **(2a)**	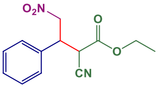 **(3a)**	6	–	69
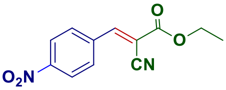 **(2b)**	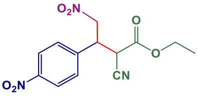 **(3b)**	5	–	72
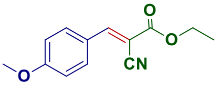 **(2c)**	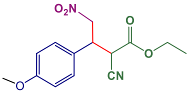 **(3c)**	5	–	70
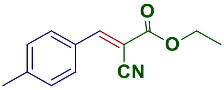 **(2d)**	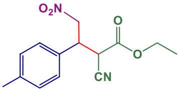 **(3d)**	6	–	67

[a] Reaction conditions: Catalyst (80.0 mg), Knoevenagel products (0.5 mmol), nitro methane (2.0 mmol), Reaction temperature, 80 °C

[b] Isolated yield

Conclusion

By introducing amino acid-like components as a base catalyst on a robust host like Fe_3O_4 NPs, we have shown that one-pot multi-step synthesis of pharmaceutically significant intermediate can be carried out sequentially. The Knoevenagel reaction can simply be carried out by base catalysis due to amino acid molecules that are present on the surface of a single nanoparticle. The product of this reaction was then condensed with nitromethane, a Michael donor, yielding a product useful in the production of numerous pharmaceutically active compounds. It can be concluded that by adopting all the optimal process parameters, (i) the developed process becomes more cost-effective than those based on bare noble metal catalysts (ii) catalyst recovery is made simple by using a magnetic field (iii) The catalyst Fe_3O_4@L-Arg is

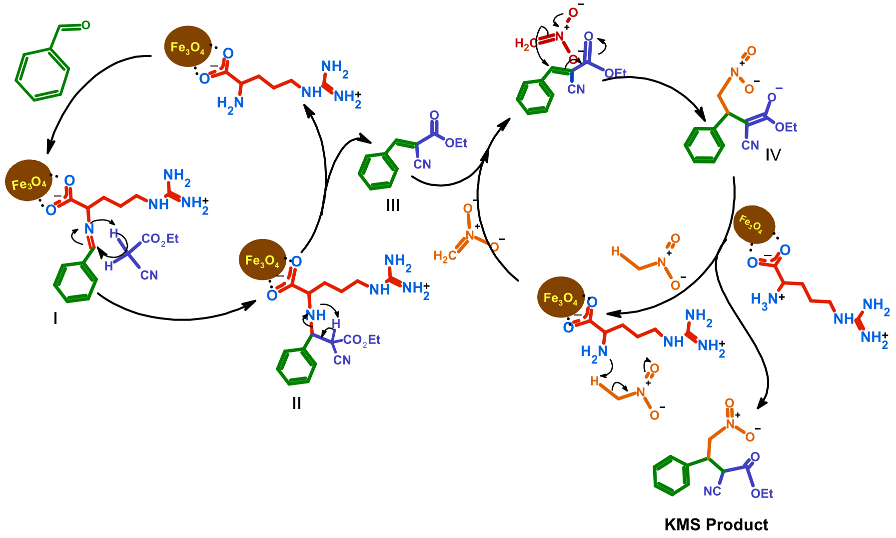

Scheme 2. Proposed mechanism for KMS in the presence of Fe_3O_4@L-Arg NPs

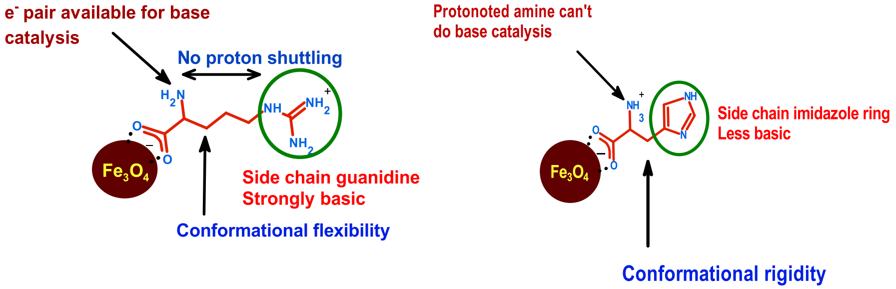

Fig. 7 Origin of difference in reactivity of Fe_3O_4@L-Arg and Fe_3O_4@L-Hist NPs catalytic systems

more effective than Fe_3O_4@L-Hist for both sequential reactions (iv) the as-synthesized catalyst Fe_3O_4@L-Arg NPs maintained its efficiency for five cycles (in this study) for 2-way catalysis (v) the reaction is "green" because no hazardous solvents are used, and the entire one-pot process can be carried out in solvent-free conditions with short reaction times, high product yields, and high activity and stability of the catalyst under the optimized reaction conditions. This work brings up new possibilities for the development of multi-component catalysts that can produce materials on a large scale while being environmentally friendly. The next investigation will focus on developing a tandem process for the mass production of enantio-pure Baclofen and Pregabalin.

Table 8 Comparative study of the efficiency of the as-synthesized catalytic systems with those previously reported for the Knoevenagel condensation reaction

Catalyst	Substrate		Conditions	Yield (%)	Refs.
[HyEtPy]Cl–H_2O–DABCO composite	4-Cl-C_6H_4-CHO	Ethyl cyanoacetate	H_2O,50 °C, 20 min	98	[51]
SiO_2-L-proline	4-NO_2-C_6H_4-CHO	Malononitrile	Acetonitrile, 80 °C, 7 h	90	[14]
	4-NO_2-C_6H_4CHO	Ethyl cyanoacetate	Acetonitrile,80 °C, 7 h	–[a]	
FeNPs/PPD@rGO	C_6H_5-CHO	Malononitrile	Toluene,40 °C, 3.5 h	100	[52]
	C_6H_5-CHO	Ethyl cyanoacetate	Toluene, 40 oC,3.5 h	23.7	
SMNPs-Amp composite	C_6H_5-CHO	Malononitrile	H_2O, RT, 4 h	99	[53]
Chol-MNPs (com)	C_6H_5-CHO	Ethyl cyanoacetate	Ethanol, RT, 24 h	79	[54]
	C_6H_5-CHO	Malononitrile	Ethanol, RT, 0.5 h	98	
Lys-Chol-MNPs	C_6H_5-CHO	Ethyl cyanoacetate	Ethanol, RT, 24 h	65	[54]
	C_6H_5-CHO	Malononitrile	Ethanol, RT, 0.5 h	96	
Gly-Chol-MNPs	C_6H_5-CHO	Ethyl cyanoacetate	Ethanol, RT, 24 h	67	[50]
	C_6H_5-CHO	Malononitrile	Ethanol, RT, 0.5 h	97	
Fe_3O_4@L-Arginine	C_6H_5-CHO	Ethyl cyanoacetate	Solvent-free, 80 °C,150 min	94	This work
Fe_3O_4@L-histidine	C_6H_5-CHO	Ethyl cyanoacetate	Solvent-free, 80 °C,180 min	91	This work

[HyEtPy]Cl–H_2O–DABCO composite—1,4-diazabicyclo [2.2.2] octane (DABCO) hydroxyl group in the ionic liquid of N-(2-Hydroxy-ethyl)-pyridinium chloride ([HyEtPy]Cl); SiO_2-L-proline- silica supported L-proline, FeNPs/PPD@rGO—p-phenylene diamine FeNPs (Iron nanoparticles) embedded onto the surface of graphene nanosheet; SMNPs-Amp composite—(aminomethyl)phenols-modified nanocatalysts; Chol-MNPs (com) -silane ligand containing choline hydroxide; Lys-Chol-MNPs—choline hydroxide function was neutralized with Lysine; Gly-Chol-MNPs—choline hydroxide function was neutralized with Glycine

[a] No reaction

Supplementary Information The online version contains supplementary material available at https://doi.org/10.1007/s11164-023-05017-3.

Acknowledgements The authors thank DST-FIST for providing NMR and BET surface area measurement facilities in the Department of Chemistry, Faculty of Science, The M. S. University of Baroda.

Authors' contributions BS contributed to methodology, validation, data curation, and formal analysis. HS contributed to writing—the original draft, conceptualization, validation, investigation, and funding acquisition.

Funding This work was financially supported by Science and Engineering Research Board (SERB), New Delhi under a sponsored scheme (No. EMR/2016/007638).

Data availability All data analyzed in this study are included in this article.

Declarations

Conflict of interest The authors declare that they have no conflict of interest.

Ethical approval This article does not contain any studies with animals performed by any of the authors.

Supplementary information The data that supports the findings of this study are available in the supplementary material of this article. HRSEM images, FTIR, UV–Vis and fluorescence, ^{1}H NMR, ^{13}C NMR spectra, and HRMS data of all the products are provided in Supplementary Materials.

References

1. M.P. van der Helm, B. Klemm, R. Eelkema, Nat. Rev. Chem. **3**, 491 (2019)
2. S.E. John, S. Gulati, N. Shankaraiah, Org. Chem. Front. **8**, 4237 (2021)
3. E. Heuson, F. Dumeigni, Catal Sci Technol. **10**, 7082 (2020)
4. S. Khaef, A. Rostami, V. Khakyzadeh, M.A. Zolfigol, A.A. Taherpour, M. Yarie, Mol. Catal. **484**, 110772 (2020)
5. A. Khazaei, A.R. Moosavi-Zare, F. Gholami, V. Khakyzadeh, Appl. Organometal. Chem. **30**, 691 (2016)
6. V. Khakyzadeh, H. Rezaei-Vahidian, S. Sediqi, S.B. Azimi, R. Karimi-Nami, Chem. Methodol. **5**, 324 (2021)
7. B. List, Chem. Rev. **107**, 5413 (2007)
8. B. List, Angew. Chem. Int. Ed. **49**, 1730 (2010)
9. P.I. Dalko, L. Moisan, Angew. Chem. Int. Ed. **43**, 5138 (2004)
10. D. Elhamifar, S. Kazempoor, B. Karimi, Catal. Sci. Technol. **6**, 4318 (2016)
11. L. Zhu, N. Lei, Z. Miao, C. Sheng, C. Zhuang, J. Yao, W. Zhang, Chin. J. Chem. **30**, 139 (2012)
12. Y. Wang, Z. Shang, T. Wu, J. Fan, X. Chen, J. Mol. Catal. A. Chem. **253**, 212 (2006)
13. A. Rahmati, K. Vakili, Amino Acids **39**, 911 (2010)
14. J. Han, Y. Xu, Y. Su, X. She, X. Pan, Catal. Commun. **9**, 2077 (2008)
15. P.S. Rao, R.V. Venkataratnam, Tetrahedron Lett. **32**, 5821 (1991)
16. B. Green, R.I. Crane, I.S. Khaidem, R.S. Leighton, S.S. Newazand, T.E. Smyser, J. Org. Chem. **50**, 640 (1985)
17. R.M. Kumbhare, M. Sridhar, Catal. Commun. **9**, 403 (2008)
18. D.S. Bose, A.V. Narsaiah, J. Chem. Res. **1**, 36 (2001)
19. M. Trilla, R. Pleixats, M.W.C. Man, C. Bied, Green Chem. **11**, 1815 (2009)
20. K. Motokura, M. Tada, Y. Iwasawa, Chem. Asian J. **3**, 1230 (2008)
21. R. Vaid, M. Gupta, Montash chem.**146**, 645 (2015)
22. M. Kolahdoozan, R.J. Kalbasi, Z.S. Shahzeidi, F. Zamani, J. Chem. 496837 (2013)
23. S. Kantevari, R. Bantu, L. Nagarapu, J. Mol. Catal. A: Chem **269**, 53 (2007)
24. V.S.R.R. Pullabhotla, A. Rahman, S.B. Jonnalagadda, Catal. Commun. **10**, 365 (2009)
25. P.M. Price, J. H. Clark, D. J. Macquarrie, J. Chem. Soc., Dalton Trans. 101 (2000)
26. J. Yu, L. Zhang, B. Cheng, Y. Su, J. Phys. Chem. **111**, 10582 (2007)
27. A. Corma, S. Iborra, I. Rodriguez, F. Sanchez, J. Catal. **211**, 208 (2002)
28. M.B. Gawande, R.V. Jayaram, Catal. Commun. **7**, 931 (2006)
29. S. Saravanamurugan, M. Palanichamy, M. Hartmann, V. Murugesan, Appl. Catal. A. **298**, 8 (2006)
30. A. Corma, R.M. Martin-Aranda, Appl. Catal. A **105**, 271 (1993)
31. T.I. Reddy, R.S. Verma, Tetrahedron Lett. **38**, 1721 (1997)
32. U.D. Joshi, P.N. Joshi, S.S. Tamhankar, V.V. Joshi, C.V. Rode, V.P. Shiralkar, Appl. Catal. A. **239**, 209 (2003)
33. A. Corma, V. Fornes, R.M. Martin-Aranda, H. Garcia, J. Primo, Appl. Catal. **59**, 237 (1990)
34. J. N. Appaturi, R. Ratti, B. L. Phoon, S. M. Batagarawa, I. Ud Din, M. Selvaraj, R. J. Ramalingam, Dalton Trans. **50**, 4445 (2021)
35. K. Komura, Y. Mishima, M. Koketsu, Appl. Catal. A: General **445**, 128 (2012)

36. E. Rodrigo, B.G. Alcubilla, R. Sainz, J.L.G. Fierro, R. Ferritto, M.B. Cid, Chem. Commun. **50**, 6270 (2014)
37. H. Ishitani, K. Kanai, Y. Saito, T. Tsubogo, S. Kobayashi, Eur. J. Org. Chem. 6491 (2017)
38. R. Jenkins, R.L. Snyder, *Introduction to X-ray Powder Diffractometry* (John Wiley & Sons, NY, 1996)
39. E. Shah, H.P. Soni, RSC Adv. **3**, 17453 (2013)
40. E. Shah E, P. Upadhyay, M. Singh, M. S. Mansuri, R. Begum, N. Sheth, H. P. Soni, New J. Chem. **40**, 9507 (2016)
41. M. Kakihana, T. Nagumo, O. Makoto, H. Kakihana, J. Phys. Chem. **91**, 6128 (1987)
42. P.S. Subramanian, P.C. Dave, V.P. Boricha, D. Srinivas, Polyhedron **17**, 443 (1998)
43. G.B. Deacon, R.J. Philips, Coord. Chem. Rev. **33**, 227 (1980)
44. T.F. Pauwels, W. Lippens, P.W. Smet, G.G. Herman, A.M. Goeminne, Polyhedron **18**, 1029 (1999)
45. A. Barth, Prog. Biophys. Mol. Biol. **74**, 141 (2000)
46. K.S.W. Sing, D.H. Everett, R.A.W. Haul, L. Moscou, R.A. Pierotti, J. Rouquerol, T. Siemieniewska, Pure Appl. Chem. **57**, 603 (1985)
47. J. Chomoucka, J. Drbohlavova, D. Huska, V. Adam, R. Kizek, J. Hubalek, Pharmacol. Res. **62**, 144 (2010)
48. L. Li, Y. Yang, J. Ding, J.M. Xue, Chem. Mater. **22**, 3183 (2010)
49. H.L. Swanson, C. Guo, M. Cao, Phys. Chem. Chem. Phys. **22**, 20349 (1998)
50. R.A. Sheldon, Green Chem. **19**, 18 (2017)
51. D. Meng Y. Qiao, X. Wang, W. Wen, S. Zhao, RSC Adv. **8**, 30180 (2018)
52. D. Patel, R. Vithalani, C.K. Modi, New J. Chem. **44**, 2868 (2020)
53. G. Wang, Z. Ding, L. Meng, G. Yan, Z. Chen, J. Hu, Appl. Organomet. Chem. **34**, e5907 (2020)
54. I. delHeirro, Y. Pérez, M. Fazardo, Mol. Catal. **450**, 112 (2018)